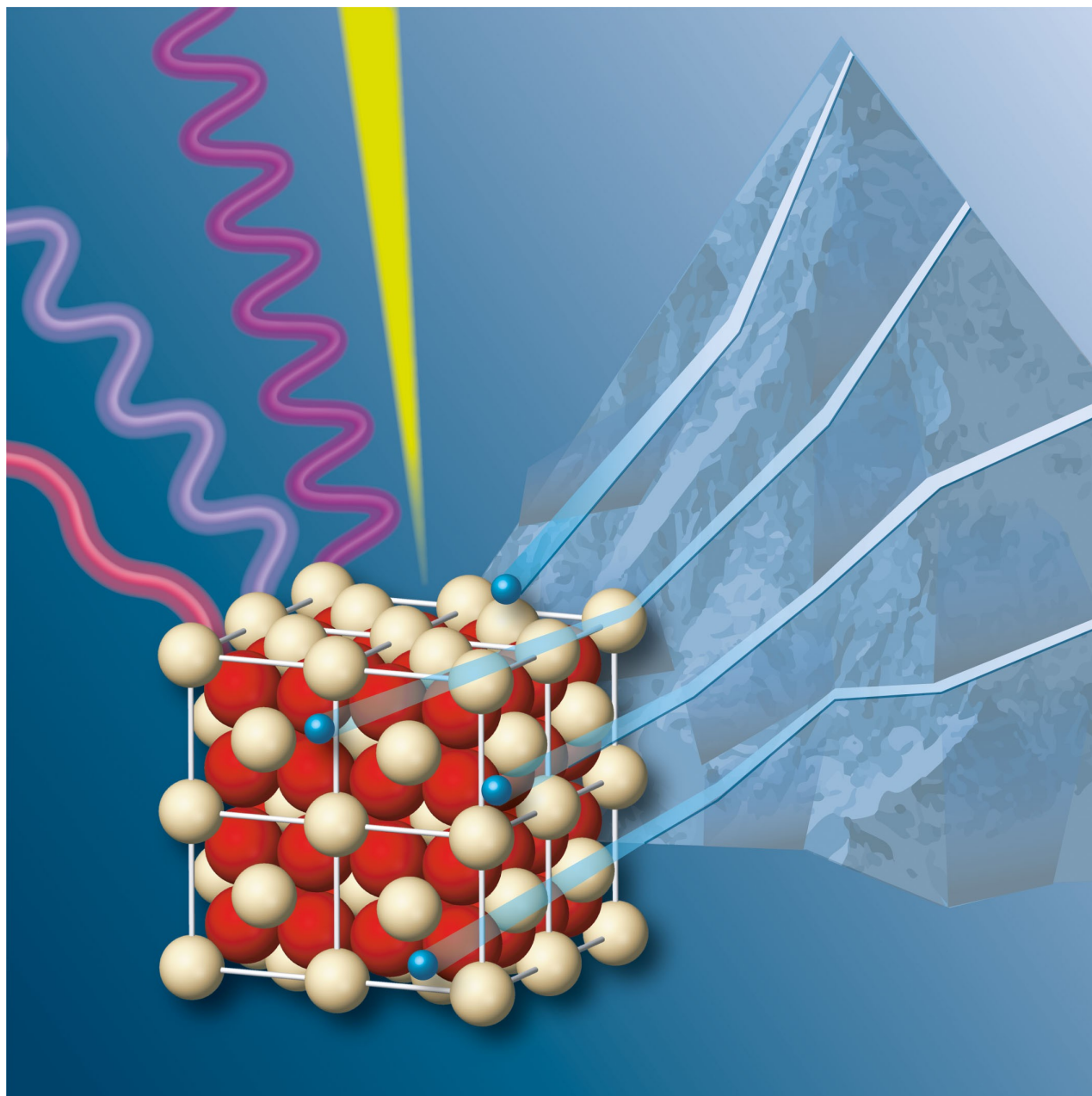


Special
Collection

Single Atom Catalysts: A Review of Characterization Methods

Matthew Kottwitz,^[a] Yuanyuan Li,^[b] Haodong Wang,^[b] Anatoly I. Frenkel,^{*,[b, c]} and Ralph G. Nuzzo^{*,[a, d]}



Single atom catalysts (SACs) harbor a potential to exceed nanoparticle catalysts in terms of activity, stability and selectivity in a growing number of chemical reactions. Although their investigation is attracting significant attention, important fundamental questions focusing on key physicochemical properties of SACs (e.g., structure – property relationships, structural dynamics, reaction-driven restructuring) remain unanswered. A main challenge for research in the field is how to reliably characterize the environments of single atoms in the presence of complicating factors such as low weight loadings, strong metal-support interactions, and atomic and multiscale hetero-

geneity of bonding in the single atom sites. This review addresses this challenge – identifying catalytically relevant features of physicochemical properties of single atoms (charge state, electronic structure, atomic configuration, bonding interactions with a support) and surveying advanced tools/methods for characterizing them. The review places a strong emphasis on multimodal methods exploiting X-ray absorption, emission and photoelectron spectroscopies, and provides several examples from the authors' research that demonstrate their use as powerful tools for SAC characterization.

1. Introduction

Single atom heterogeneous catalysts (SACs) have attracted much attention in the last decade, primarily because they have shown high activity, selectivity, and stability in a growing number of chemical reactions.^[1] After the concept of a SAC was first introduced by T. Zhang and co-workers,^[2] their investigation experienced rapid growth in fields spanning diverse forms of heterogeneous catalysis including notable examples of thermolytic, photo, and electro catalysis. The embodiments of bonding and composition in SAC materials are both complex and diverse, having evolved well beyond the embedding of isolated atoms at the interface of an active host matrix (mostly those of metal oxides) in the early stages of their investigation to metals (giving rise to single atom alloys, or SAAs^[11]), metal organic frameworks, carbon nitride and other organic framework-based materials, among many others.^[3] Current research in the field continues to expand the range of SAC structures with useful activities and selectivity in catalytic transformations as shown in Figure 1. The diversity of these exemplary SACs

ranges from single metal atoms anchored on the surface of a mesoporous reducible oxide^[4] (Figure 1a) to isolated surface metal atoms as part of an alloy^[5] (Figure 1b) to metal atoms supported on single layer materials^[6] (Figure 1c). While “single atom catalysts” is the ubiquitous term used to describe these systems, the phrase “atomically dispersed catalysts” may better convey that the individual metal atoms are located at the surface of another material. There are several earlier reviews that have explored recent developments in studies of SAC activity, such as capturing reaction intermediates and monitoring the dynamics of both the geometric structure and electronic

- [a] M. Kottwitz, Prof. R. G. Nuzzo
Department of Chemistry
University of Illinois
Urbana, IL 61801 (USA)
E-mail: r-nuzzo@illinois.edu
- [b] Dr. Y. Li, H. Wang, Prof. A. I. Frenkel
Department of Materials Science and Chemical Engineering
Stony Brook University
Stony Brook, NY 11794 (USA)
E-mail: anatoly.frenkel@stonybrook.edu
- [c] Prof. A. I. Frenkel
Division of Chemistry
Brookhaven National Laboratory
Upton, NY 11973 (USA)
- [d] Prof. R. G. Nuzzo
Surface and Corrosion Science, School of Engineering Sciences in Chemistry,
Biotechnology and Health
KTH Royal Institute of Technology
Drottning Kristinasväg 51
100 44 Stockholm (Sweden)

Special Collection An invited contribution to a joint Special Collection between Batteries & Supercaps and Chemistry-Methods on In Situ and Operando Methods for Energy Storage and Conversion. Please visit chemistry-methods.org/collections to view all contributions.

© 2021 The Authors. Published by Wiley-VCH GmbH. This is an open access article under the terms of the Creative Commons Attribution Non-Commercial License, which permits use, distribution and reproduction in any medium, provided the original work is properly cited and is not used for commercial purposes.

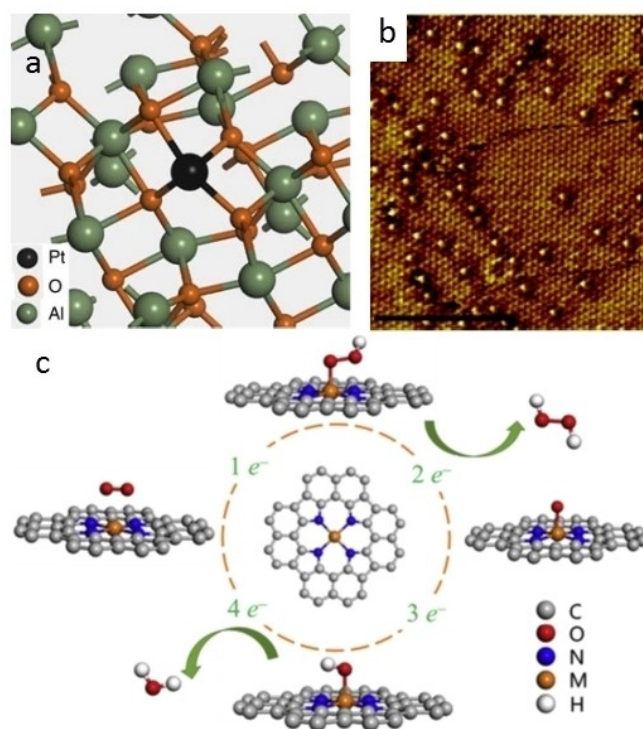


Figure 1. (a) Schematic of single atom Pt anchored on mesoporous Al₂O₃ for use in the selective hydrogenation of 1,3-butadiene. Reproduced with permission from ref. [4]. Copyright, 2017, The Author(s). (b) STM image of isolated Pd atoms substituted into a Cu surface layer for selective hydrogenation (5 nm scale bar). Reproduced with permission from ref. [5]. Copyright, The Royal Society of Chemistry. (c) Schematic of the Oxygen Reduction Reaction (ORR) for transition metal single atom catalysts anchored in N-doped graphene. Reproduced with permission from ref. [6]. Copyright, 2019 published by Elsevier Inc.

environment of atomically dispersed sites,^[7] and optimizing their reactivity by tailoring the local environment of active sites and speciations of the metal ions they embed.^[8] Similar advances in the use of SACs for electrocatalysis have also been reviewed.^[9] In general terms, progress in the SAC field has gone hand in hand with an increasing recognition of the various forms of complexity that are exhibited by these materials – initially unexpected due to the assumed “homogeneity” of their atomically dispersed sites. As such, unveiling the structure–property relationships in SACs is hindered by both the inherent heterogeneity of the metal sites present in SACs and the paucity of experimental methods capable of probing the attributes of their bonding structures with adsorbates and support in presence of such heterogeneity.

Several recent reports summarized specific methods, such as extended X-ray absorption fine structure (EXAFS) spectroscopy for studying coordination environments in Pt SACs on diverse supports.^[10] The literature also describes useful methods for probing electronic structures associated with metal–support interactions in SACs.^[11] In this review, we discuss in depth the characterization techniques for single atom catalysts, focused on addressing key chemical questions: What structural, dynamic and electronic attributes of SACs affect their activity, selectivity, stability and, in general, catalytic reaction mechanisms? To address these questions, we outline methods, and their combinations, that are effective for characterizing speciations of SACs, measure oxidation states of metal and support atoms,

characterize their electronic structure and properties, and provide quantitative information about the local bonding/coordination environments. We also highlight the implications of coexisting multiple binding sites for SACs that complicate interpretation of ensemble averaging techniques, such as EXAFS spectroscopy. The sections below develop these points in turn and demonstrate how multimodal methods are usefully integrated to characterize them.

2. Properties and Approaches to their Characterization

2.1. Oxidation States of Metal and Support Atoms

Characterization of oxidation states of SACs and support atoms comprising their nearest environment is essential to probe the nature of the metal–support interactions that are now understood to highly impact the stability and activity of supported SACs. The correlation between metal loadings, surface defects, and the oxidation states of single atoms on a support has been widely investigated.^[12] Single metal atoms may show different oxidation states at different coordination environments, as shown in Figure 2a. Ye et al.,^[7] prepared two types of ceria nanorod supports with two different concentrations of Ce³⁺ surface defect sites (noted as x%Pt₁/D–CeO₂ with relatively



Matthew Kottwitz obtained his B.S. degree from the University of Nebraska-Lincoln in 2015, majoring in Chemistry and Mathematics. He is currently a fifth-year Ph.D. student at the University of Illinois at Urbana-Champaign under the supervision of Prof. Ralph G. Nuzzo. His research focuses on characterizing the geometric and electronic structure of single atom catalysts with applications in the energy industry.



Yuanyuan Li obtained her Ph.D. degree from the University of Science and Technology of China. She is currently a research scientist and working in Prof. Anatoly Frenkel's group in the Department of Materials Science and Chemical Engineering at the Stony Brook University. Her research focuses on establishing structure–property relationships for rational design of catalysts.



Haodong Wang graduated from Shanghai Jiao Tong University, China, in 2019, majoring in Materials Science and Engineering. He joined Prof. Anatoly Frenkel's group as a Ph.D. student at Stony Brook University in 2019. His research focuses on structure and stability of supported single atom catalysts.



Anatoly Frenkel is a Professor in the Department of Materials Science and Chemical Engineering at the Stony Brook University and a Senior Chemist (Joint Appointment) at the Division of Chemistry, Brookhaven National Laboratory. He received M.Sc. degree from St. Petersburg University and Ph. D. degree from Tel Aviv University, all in Physics, followed by a postdoctoral appointment at the University of Washington. His research interests focus on development and applications of in situ and operando synchrotron methods to solve a wide range of materials problems, with most recent emphasis on catalysis, electromechanical materials, filtration materials, quantum dots, as well as machine learning methods for structural analysis and design of functional nanomaterials. He is a Fellow of the American Physical Society.



Ralph Nuzzo is the G. L. Clark Professor of Chemistry and Professor of Materials Science at the University of Illinois, and Professor of Materials Chemistry at the KTH Royal Institute of Technology in Stockholm Sweden. Professor Nuzzo received an AB degree in Chemistry from Rutgers and earned a Ph.D. from MIT in 1980. He was a Member of Technical Staff in Research at Bell Laboratories, where he was named a Distinguished Member of the Staff in Research. He is a fellow of the American Academy of Arts and Sciences, the AAAS, the ACS, the AVS, and the RSC.

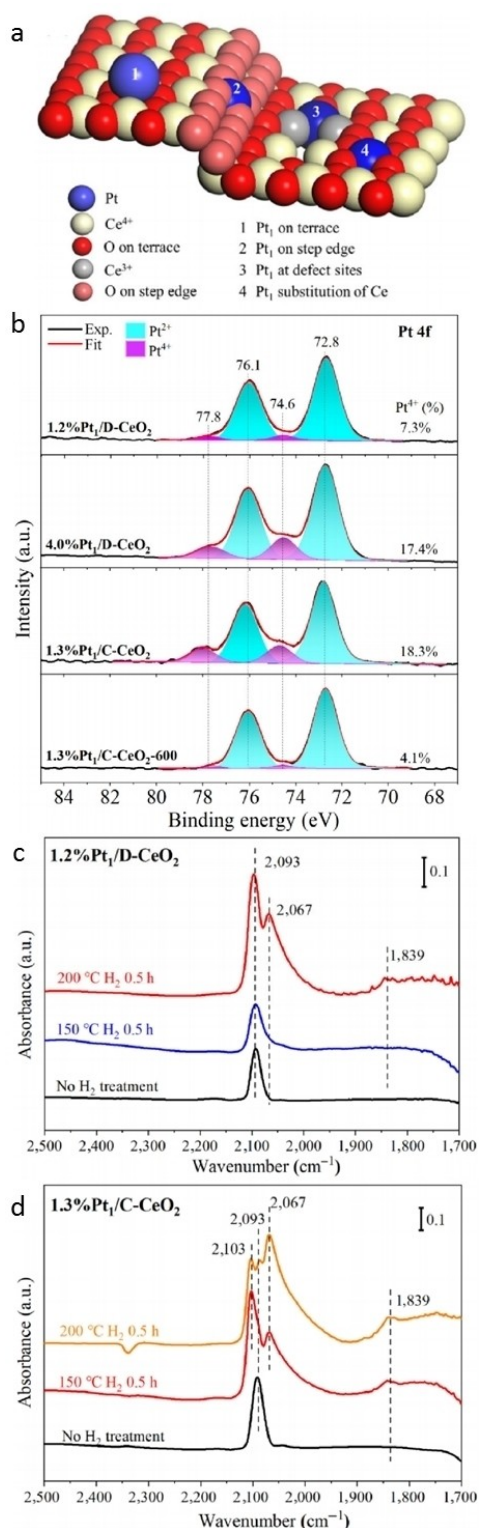


Figure 2. (a) Schematic model of CeO₂ supported Pt single atom placement with different local coordination structures. (b) XPS spectra of the Pt/CeO₂ SACs in the Pt 4f region. DRIFTS of CO chemisorption on (c) 1.2%Pt₁/D-CeO₂ and (d) 1.3%Pt₁/C-CeO₂ at the CO saturation coverage. (D-CeO₂ support contains 25% Ce³⁺ species and C-CeO₂ support contains 18% Ce³⁺ species). Figure 2. (a–d), reproduced with permission from ref. [7]. Copyright, 2019 Tsinghua University Press and Springer-Verlag GmbH Germany, part of Springer Nature.

higher Ce³⁺ components and x%Pt₁/C-CeO₂ with relatively lower Ce³⁺ components). X-ray photoelectron spectroscopy (XPS) results shown in Figure 2b indicated that Pt atoms anchored on defect sites are mainly in a Pt²⁺ valence state, while those on terrace sites are mainly in a Pt⁴⁺ state. Additionally, Kunwar et al.^[13] found that Pt species in ceria supported Pt single atom catalysts with high Pt loading (3 wt.%) were primarily in the Pt²⁺ oxidation state with a fraction of Pt⁴⁺ also being observed. When the Pt loading was increased to 4 wt.%, an obvious metallic Pt peak coexisting with the ionic Pt²⁺ was observed. Contributions from Pt⁴⁺ speciations were not observed at the higher loading, indicating that metal composition can influence the oxidation states adopted by isolated Pt atoms on the support. The contradictory impact of increased Pt weight loading on the observed oxidation states as seen in the two aforementioned studies illustrates the role that the method of deposition and the particular surface facets of the support material play in determining the resultant metal speciations. The ability to form different oxidation states offers an interesting opportunity to investigate the properties of such varying types of single atom catalysts. The diffuse reflectance infrared Fourier transform spectroscopy (DRIFTS) results shown in Figure 2c and d proved the presence of Ce³⁺ in CeO₂ support can improve the stability of Pt single atoms on CeO₂. That is, the 1.2%Pt₁/D-CeO₂ sample with higher surface Ce³⁺ fraction does not display a peak at 2067 cm⁻¹ indicative of aggregation when treated with H₂ at 150 °C for 30 minutes. This result is consistent with a previous study in which noble metals were found to preferentially nucleate growth of small clusters at the defects and/or edge sites of crystalline CeO₂(111) films.^[14] As these data suggest, the presence of defect sites, for example Ce³⁺ sites in a CeO₂ support, leads to strong Pt–O–Ce bonding interactions, providing a potentially useful way to improve the stability of single atom catalysts.

The activity of single atom catalysts in reaction conditions is closely related to the oxidation states of metal and support atoms. Chen et al.^[15] reported that Pt single atoms stabilized by Ce³⁺ defective sites on porous CeO₂ had superior catalytic activity for CO oxidation. To explore the role of Pt single atoms in the CO oxidation process, they conducted XPS tests that revealed they mainly present as Pt²⁺ in the active working state. The core level spectra for the precatalyst, dubbed CeO₂-AA-Pt-cal (a higher Ce³⁺ content, calcined (cal) sample consisting of Pt deposited on CeO₂ nanorods following treatment with L-(-)-ascorbic acid (AA)) before use for CO oxidation, are shown in Figure 3a. After its use for CO oxidation, the Pt present was partially reduced from Pt²⁺ to Pt⁰, as shown in Figure 3b. By contrast, the Pt species in CeO₂-IMP-Pt (a sample consisting of Pt deposited on CeO₂ nanorods via traditional incipient wetness impregnation approach) consisted mainly of Pt⁰ before CO oxidation induced a higher Pt⁴⁺ oxidation state. These results and the improved catalytic activity observed for the CeO₂-AA-Pt-cal sample relative to the CeO₂-IMP-Pt sample suggest that oxidation of Pt species may lead to decreased catalytic activity. Other results, however, seem to disagree with this conclusion. From the study of Ye et al.,^[7] 1.2%Pt₁/D-CeO₂ (with higher Pt²⁺ content) was found to show higher activity

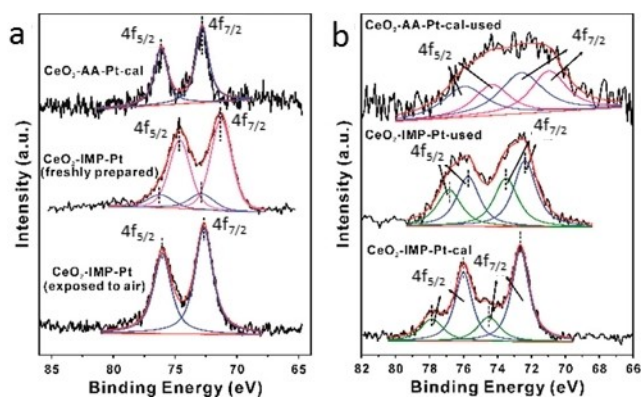


Figure 3. (a) XPS spectra and corresponding fitting curves of Pt 4f in the CeO₂-AA-Pt-cal and CeO₂-IMP-Pt. (b) XPS spectra and corresponding fitting curves of Pt 4f in the CeO₂-AA-Pt-used, CeO₂-IMP-Pt-used, and CeO₂-IMP-Pt-cal. The -used sample representing that Pt/CeO₂ is measured after time on stream test. Reproduced with permission from ref. [15]. Copyright 2018 American Chemical Society.

than that of 1.3%Pt₁/C-CeO₂ in dry CO oxidation, while it has an opposite trend in water-mediate CO oxidation. The CeO₂ nanorods used as a support in this study are denoted D-CeO₂ for nanorods simply dried at 60°C overnight and C-CeO₂ for those treated with subsequent calcination. Ye et al., noticed that 4.0%Pt₁/D-CeO₂ and 1.3%Pt₁/C-CeO₂ with high activities in water-mediated CO oxidation reaction both contained considerable amounts of Pt⁴⁺, thus implying that the Pt⁴⁺ might contribute to the high activity noted, in a seeming contradiction to the results of the study by Chen et al.^[15] Therefore, these combined results lead to a conclusion that the oxidation states of metal and supports are not the only parameters that combine to dictate the activities of single atom catalysts.^[16] There are other parameters that will also contribute to the activity of SACs. Prof. T. Zhang's research group^[17] illustrated the correlation between catalytic activity and oxidation state with the coordination number (CN) of Pt in the first Pt-O shell. It is interesting that their results indicate that the smaller the Pt-O CN is, the lower the oxidation state is of the Pt single atoms, and the higher their associated catalytic activity. Such a structure-activity relationship demonstrates well that the catalytic performance of SACs can be optimized via altering the oxidation state and local coordination environment, as will be discussed in greater detail later.

The mechanisms of single atom catalytic systems for many reaction types (a notable example is CO oxidation) are still under intensive debate.^[18] In-situ investigations of SACs that can follow changes of their oxidation states in a full catalytic cycle are required to understand the roles of the metal and support during the process. The use of in situ or operando measurements may better elucidate the investigated chemical property, but care must be taken to interpret the results within the correct context. Hulseley et al.^[19] conducted in situ DRIFTS and XPS experiments to investigate the active site of an atomically dispersed Rh on phosphotungstic acid catalyst (Rh₁/NPTA) that exhibits an onset temperature of 423 K during CO oxidation. The CO DRIFTS results (Figure 4a), reveal the trans-

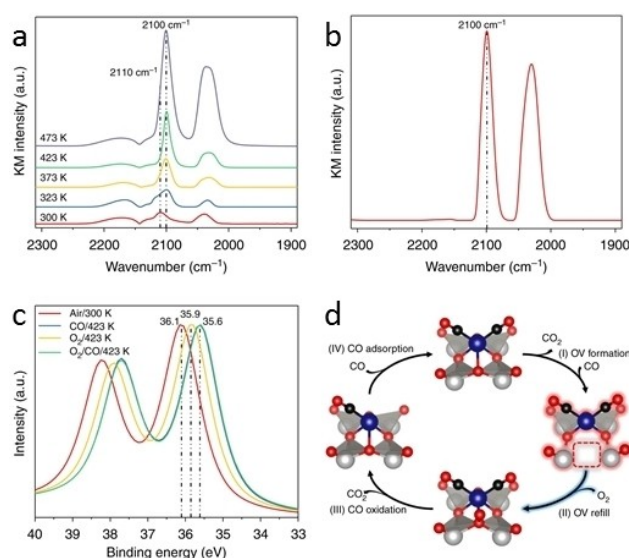


Figure 4. In situ DRIFT and XPS spectroscopies and proposed reaction cycle. CO DRIFT spectra of (a) Rh₁/NPTA catalyst under CO at increasing temperatures (from bottom to top) and (b) of the catalyst under CO/O₂ at 473 K. (c) In situ W 4f_{7/2} XPS spectra of the support under different gas atmospheres and temperatures. (d) Key steps of the proposed reaction mechanism based on in situ spectroscopy; the steady-state catalyst structure and the corresponding rate-controlling step are highlighted. Atom colors: W (gray), O (red), C (black), Rh (blue); OV stands for oxygen vacancy. Figure 5. (a–d), reproduced with permission from ref. [19]. Copyright 2019, The Author(s).

formation of Rh(CO)₂³⁺ species to a Rh(CO)⁺ speciation upon exposure to CO in a temperature programmed reaction. In detail, a redshift of the band from 2110 cm⁻¹ (assignable to Rh(CO)₂³⁺ species) to 2100 cm⁻¹ (assignable to Rh(CO)₂⁺ species) was observed beginning at 323 K. This experiment strongly suggests Rh⁺ species are dominant in CO oxidation under reaction conditions (Figure 4b). Correlated XPS results of W 4f_{7/2} spectra indicate the support is actively contributing to the oxidation of CO and that a reduction of tungsten in the support occurs at 423 K (Figure 4c). Under an O₂ atmosphere, the tungsten species are gradually re-oxidized. Exposing the catalyst to a mixture of O₂ and CO leads to an immediate reduction of the tungsten species to ones exhibiting a W 4f_{7/2} binding energy of 35.6 eV, a result further confirming the existence of support-associated oxygen vacancies during reaction conditions. Their in situ DRIFTS and XPS results provide further evidence to support the proposed catalytic cycle (Figure 4d), where Rh cycles between Rh³⁺ and Rh⁺ and that the structure associated with oxygen vacancies is the dominant working state of the catalyst. As shown in this example, a combination of in situ DRIFTS and XPS techniques which indicate oxidation states of both metal and support atoms can provide clues on how single atom catalysts work at a molecular level in a full catalytic cycle.

As illustrated above, DRIFTS and XPS are complementary techniques, ones providing distinct sensitivities with which to investigate features of bonding and oxidation states of metal and support atoms in SACs. DRIFTS is an infrared spectroscopy technique which is commonly used in the field of catalysis to identify adsorbed species and monitor how they change as a

reaction proceeds, giving insights into the stability, homogeneity and oxidation state of the active species.^[20] As an adsorbate CO is often used as a probe molecule in DRIFTS studies to monitor the dispersion and oxidation state of exposed noble metal sites on supported catalysts.^[2] In a previous study,^[21] we employed CO DRIFTS to compare both ceria supported Pt SAC and nanocluster PtO_x materials. All the characteristic peaks appear between 1700 and 2300 cm⁻¹ and can be assigned to different vibrational/stretching modes of CO adsorbed on Pt sites (Figure 5a). The $\nu(\text{CO})$ frequency is sensitive to the Pt coordination and shifts to lower frequencies when the Pt coordination decreases.^[22] The peak at 2170 cm⁻¹ is due to gas-phase molecules, and disappears after the CO is flushed away. The retained species demonstrate a nominally stronger bond form of the adsorbate. The single narrow peak appearing at 2090 cm⁻¹ in Pt SACs corresponds to bonding interactions of CO on a higher valence (Pt^{δ+}) site. In contrast, the additional shoulder centered at 2045 cm⁻¹ seen for the PtO_x clusters indicates an atop bonded CO molecule on Pt⁰. Thus, CO DRIFTS is a convenient characterization technique to differentiate ionic Pt single atom states from metallic (zerovalent) Pt sites within nanoclusters. These assignments are inferential, however, with more rigorous assignments for the formal oxidation states of the Pt present in each case coming with data from XPS studies.

XPS is a universal characterization technique for probing the chemical and compositional properties of the catalyst surfaces. Its quantitative accuracy and precision can satisfy the requirements for supported metal single atom catalysts.^[17,23] In the case of the ceria supported SAC and PtO_x samples noted above, Pt 4f core level data for each are presented in Figure 5b. For the PtO_x cluster sample, contributions from both of Pt²⁺ and Pt⁰ oxidation states are required to fit the experimental data. It is

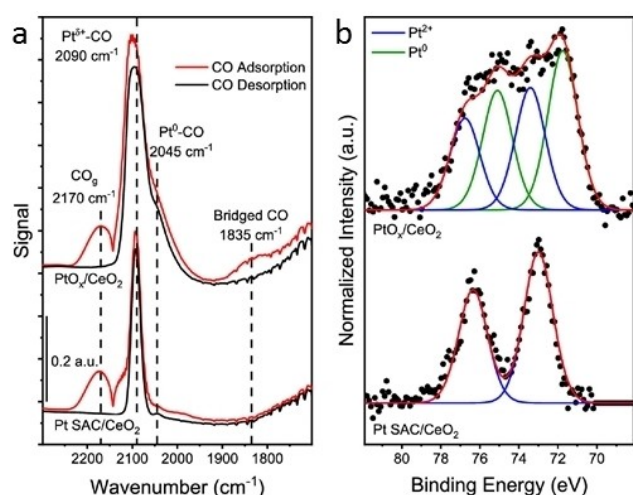


Figure 5. (a) DRIFT spectra after CO adsorption (red) and CO desorption (black) of PtO_x clusters on CeO₂ (incipient wetness sample) and Pt single atoms on CeO₂ (sol-impregnation sample). Characteristic peaks for CO in the gas-phase (2170 cm⁻¹), adsorbed atop Pt^{δ+} or Pt⁰ (2090 and 2045 cm⁻¹, respectively), and bound to a bridge site (1835 cm⁻¹) are noted. (b) The Pt 4f region of XPS spectra for the PtO_x cluster and Pt single atom samples with Pt²⁺ (blue) and Pt⁰ (green) fitting curves. Reproduced with permission from ref. [21]. Copyright 2019 American Chemical Society.

necessary to mention that the observed binding energy of the Pt 4f_{7/2} core level for the Pt⁰ species is 71.5 eV and 73.1 eV for Pt²⁺ species, which are slightly higher than those reported for reference compounds. It has been shown in other literature^[24] that both support and particle size could induce positive binding energy shifts of Pt nanostructures because of the reduction of effective atomic coordination numbers. For Pt SACs, there is no evidence of Pt⁰ sites, confirming the homogeneity of Pt²⁺ sites in the latter sample. The quantitative XPS analyses shown in the figure provide an effective means through which to evaluate the ratio of different Pt species present in each case.

The complementarity of DRIFTS and XPS arises in how they differ in the manner of what attributes of the catalytic system they probe (as described above), and in their penetration depths. As a spectroscopic probe, the CO-DRIFTS technique relies on adsorbed CO on the surface of a material, which in turn is sensitive to the nature of adsorption sites and other features of surface structure.^[25] Therefore, it can only probe the atoms located at surface layer and the point of binding, which is also most relevant for catalysis. By contrast, XPS data are obtained by irradiating a sample surface with a beam of X-rays, which can excite photoelectron emission detectable up to a depth of ~10 nm, depending on X-ray energy.^[26] Generally therefore, a combination of XPS and DRIFTS studies will be required to provide a more complete understanding of the oxidation state and bonding features of SACs than either technique can provide independently.

2.2. Electronic Structure

With a decrease of the number of metal atoms in a particle, the electronic bands become narrower and are, eventually, replaced by discrete states. For single atoms in the gas phase, characteristically sharp features of atomic orbitals are observed.^[27] When single atoms are dispersed onto supports, features in the density of d-states of single atoms become broader. The extent of the broadening depends on the single atom-host interaction. For example, as shown in Figure 6(a), for Cu host, the features in the d-band density of states of Pt/Pd/Ir/Rh/Ni single atoms appear to be broader than Ag-based ones. For Cu and Pt, the broadening is more significant due to the inherent immiscibility between these two metals.^[27] For single atom alloys, the d-band center and width (Figure 6(b)) are linearly correlated as observed in bulk metal alloys (for which the overall d-band filling stays approximately constant), suggesting that the single atom alloys are metallic in nature.^[27]

For monometallic systems, a d-band model is often used to explain physicochemical features of adsorbate bonding.^[28] The essence of the d-band model is as follows. The metal d states hybridize with the adsorbate states to form bonding and antibonding states. For the metals, the bonding state is full. The ability to fill the antibonding state is determined by the energy difference, Δ , of the antibonding state and the Fermi level. An increased filling of the antibonding state (corresponding to the lowering of Δ) causes weakening of metal-adsorbate interac-

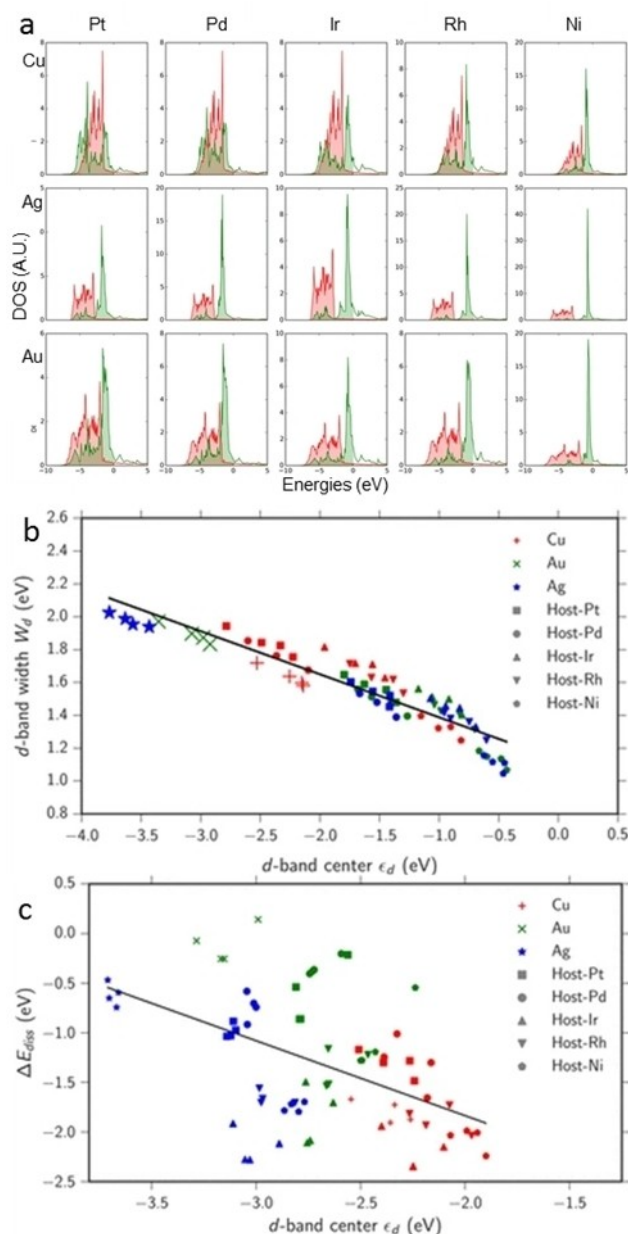


Figure 6. (a) d-Band density of states for the fcc(111) single atom alloy surfaces. Pt/Pd/Ir/Rh/Ni (green) are single atoms in the alloy and Cu/Ag/Au (red) are host metals. (b) d-Band width versus the d-band center for the dissociative adsorption of hydrogen on fcc(111), (100), and (211) pure metal surfaces and single atom alloy surfaces. The points corresponding to Cu, Au, and Ag surfaces are in red, green and blue, respectively. A single atom alloy is depicted by a colored shape, as defined in the figure legend. (c) Dissociative energy of adsorption of hydrogen on the single atom alloys and host metals and the d-band center. The linear fit is given by the solid line and serves as a visual aid. Figure 6. (a–c), reproduced with permission from ref. [27]. Copyright 2018, Springer Science Business Media, LLC, part of Springer Nature.

tion. Experimentally therefore, the location of the d states center can be used to predict the bond strength. However, this model is unlikely to be applicable to single atom systems. As shown in Figure 6(c), for single atom alloys, the correlation between the dissociative energy of adsorption of a hydrogen molecule and the d-band center does not follow a linear scaling

relationship. This suggests that any correlations as exist between the d-band characteristics of a single atom alloy and its catalytic properties could be more complicated.

A nonlinear relationship between the d band characteristics and catalytic properties is also observed in oxide-supported single atoms. To study structure-property relationships, Li et al. studied Pt single atoms dispersed on different oxide supports (Co_3O_4 , ZrO_2 , CeO_2) and graphene.^[29] The $\text{Pt}_1/\text{Co}_3\text{O}_4$ system, for example, shows improved activity (up to 68-fold higher than those on other supports) and a notable stability in the dehydrogenation of ammonia borane (for low-temperature hydrogen generation). The reactivity of other samples fell in the order $\text{Pt}_1/\text{Co}_3\text{O}_4 > \text{Pt}_1/\text{graphene} > \text{Pt}_1/\text{ZrO}_2 > \text{Pt}_1/\text{CeO}_2$ with an order of stability of $\text{Pt}_1/\text{Co}_3\text{O}_4 > \text{Pt}_1/\text{CeO}_2 > \text{Pt}_1/\text{ZrO}_2 > \text{Pt}_1/\text{graphene}$. Experimentally, the electronic/atomic structures of the catalysts were characterized by using X-ray absorption spectroscopy (XAS), DRIFTS and XPS. The white line of Pt L_3 edge, which corresponds to the transition of 2p electrons to unoccupied 5d valence orbitals, shows higher white line peak intensities that directly correlate with the population of unoccupied Pt 5d states. As shown in Figure 7(a), for the population of unoccupied Pt 5d states falls in the order $\text{Pt}_1/\text{Co}_3\text{O}_4 > \text{Pt}_1/\text{ZrO}_2 > \text{Pt}_1/\text{CeO}_2 > \text{Pt}_1/\text{graphene}$. This provides an explicit electronic correlation against which to judge the qualitative features of reactivity described above.

The DRIFTS spectra recorded using CO as a probe also provide information on occupancies of the metal 5d states and confirm the trends seen in XPS data.^[29] As shown for $\text{Pt}_1/\text{Co}_3\text{O}_4$ in Figure 7(c), the peak for atop adsorbed CO appears at a higher wavenumber value compared to that of Pt_1/CeO_2 and Pt_1/ZrO_2 , which suggests that in $\text{Pt}_1/\text{Co}_3\text{O}_4$ the Pt single atoms have less populated 5d state electrons which in turn weakens the $\text{Pt}(5d)-\text{CO}(2\pi^*)$ bonding through π backdonation.^[29] EXAFS analyses (Figure 7(b)) show that for the coordination number of Pt–O, $\text{Pt}_1/\text{Co}_3\text{O}_4 > \text{Pt}_1/\text{CeO}_2 > \text{Pt}_1/\text{ZrO}_2 > \text{Pt}_1/\text{graphene}$. XPS results (Figure 7(d)) suggest that for the $\text{Pt}^{4+}:\text{Pt}^{2+}$ ratio: $\text{Pt}_1/\text{Co}_3\text{O}_4 > \text{Pt}_1/\text{ZrO}_2 > \text{Pt}_1/\text{CeO}_2$.^[29] By correlating all these trends, it is seen that for these oxide supported systems, the reactivities are correlated with both the population of unoccupied Pt 5d states and the oxidation state of Pt. The catalyst with the higher average Pt oxidation state or larger population of unoccupied Pt 5d states shows higher reactivity in dehydrogenation of ammonia borane.

Theoretically, DFT calculations were performed to study the features of Pt 5d orbitals. As shown in Figure 7(e), in $\text{Pt}_1/\text{Co}_3\text{O}_4$, for the spin-up and spin-down components, the unoccupied 5d states locate at different places: one is at 0.39 eV (the spin-up) and the other is at 0.26 eV above the Fermi level. Such differences could not be found in other Pt single atom systems with non-magnetic supports. For the center of the unoccupied 5d states, $\text{Pt}_1/\text{ZrO}_2 > \text{Pt}_1/\text{CeO}_2 > \text{Pt}_1/\text{Co}_3\text{O}_4 > \text{Pt}_1/\text{graphene}$. It seems that for the oxides supported systems, the center of the unoccupied 5d states could not be directly correlated with catalytic reactivity of the Pt single atom catalysts. The non-symmetric Pt 5d states, due to the interaction between single atoms and magnetic supports, may play additional roles here. Similar results were also reported by Chen et al.^[30] who studied

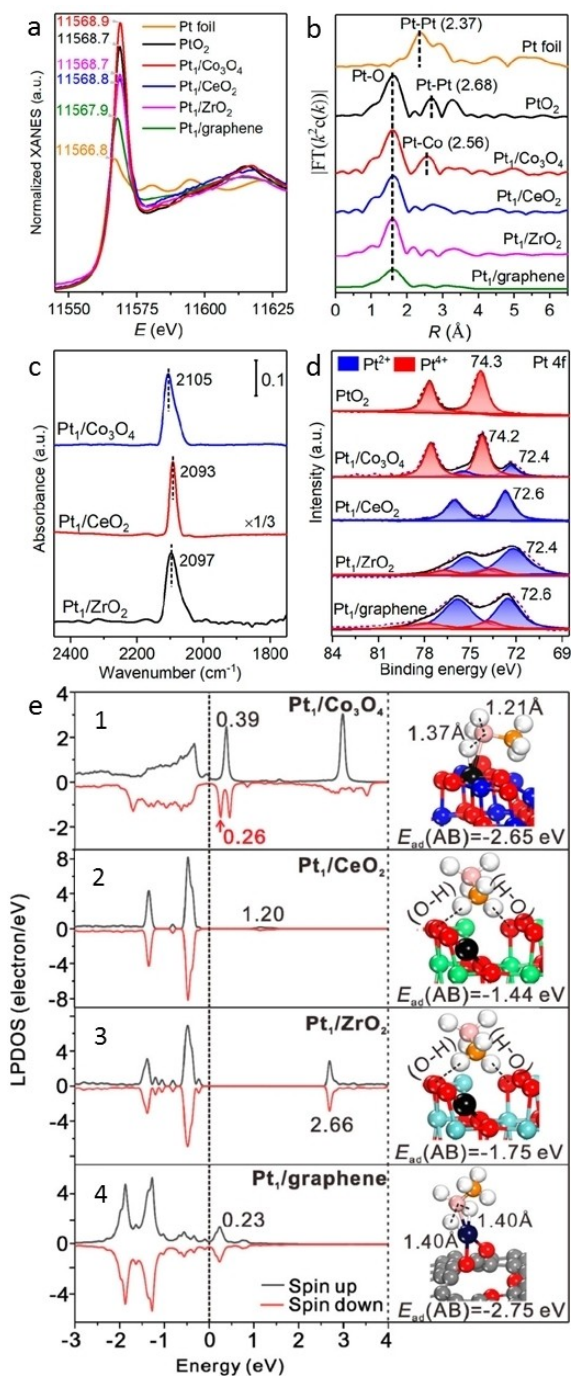


Figure 7. (a–d) Experimental characterization of Pt single atoms. (a) XANES spectra of Pt₁/Co₃O₄, Pt₁/CeO₂, Pt₁/ZrO₂, and Pt₁/graphene SACs as well as the Pt foil and PtO₂ reference at the Pt L₃-edge. (b) The corresponding k^2 -weighted Fourier transform spectra. (c) DRIFTS of CO chemisorption on Pt₁/Co₃O₄, Pt₁/CeO₂, and Pt₁/ZrO₂ at the saturation coverage. (d) XPS spectra of Pt₁/Co₃O₄, Pt₁/CeO₂, Pt₁/ZrO₂, Pt₁/graphene, and PtO₂ in the Pt 4f region. (e) Local partial density of state (LPDOS) projected on the Pt₁ 5d orbitals with the Fermi level set at zero and the local configurations for AB adsorption. From top to bottom: Pt₁/Co₃O₄, Pt₁/CeO₂, Pt₁/ZrO₂, and Pt₁/graphene. The gray, white, pink, orange, red, green, dark blue, sky blue, and black spheres represent carbon, hydrogen, boron, nitrogen, oxygen, cerium, cobalt, zirconium, and platinum, respectively. The adsorption energy of AB on these Pt₁ SACs is also indicated. Figure 7. (a–e), reproduced with permission from ref. [29]. Copyright 2019, American Chemical Society.

amorphous Fe₂O₃ 2D nanosheets variously supporting Pt single atoms, Pt clusters and Pt nanoparticles and found a direct correlation between metal-support charge transfer and their catalytic activity for CO oxidation: the higher the charge transfer, the lower the adsorption energy of CO, the higher the adsorption energy of O₂, and consequently, the higher the reactivity for CO oxidation. The results also show a nonlinear correlation exists between the d band center of the Pt species and the catalytic properties evidenced.

Several groups have explored possible nonlinear factors related to the stability of single atom systems and proposed models to make correlations between the adsorption energy (E_{ads}) and key properties of metals/supports.^[31] Those nonlinear terms arise from combinations of physical properties which include the coordination of the support metal in the bulk, the electron affinity of the metal, the ionization energy of the metal, the ionization potential of the oxide support, the band gap of the oxide support, oxidation enthalpy of the metal, the LUMO of the metal and support, the experimental bond dissociation energy of the M–O dimer, the group number and number of d-electrons and the d-band center of the supported metal atom.

As noted above, for studies of the electronic structure of single metal atoms, X-ray absorption near edge spectroscopy (XANES) measurements are particularly useful as seen in the exemplary case reported by Li, et al. (Figure 7(a)).^[29] In addition to XANES, resonant inelastic X-ray scattering (RIXS) provides an additional and powerful tool through which to image such valence d state features. The RIXS process includes two steps that we can illustrate schematically taking Pt metal as an example.^[32] In the first step, the incident photon excites a core level Pt 2p electron to unoccupied Pt 5d valence states, leaving a hole in the core level. In the second step, an electron from the occupied region of the Pt 5d valence state fills the core hole, producing the photon emission that yields the final state configuration. The RIXS planes therefore provide information of both the unoccupied and occupied regions of the Pt 5d states. The main features observed in the RIXS planes (Figure 8) are due to the transition between occupied and unoccupied Pt 5d

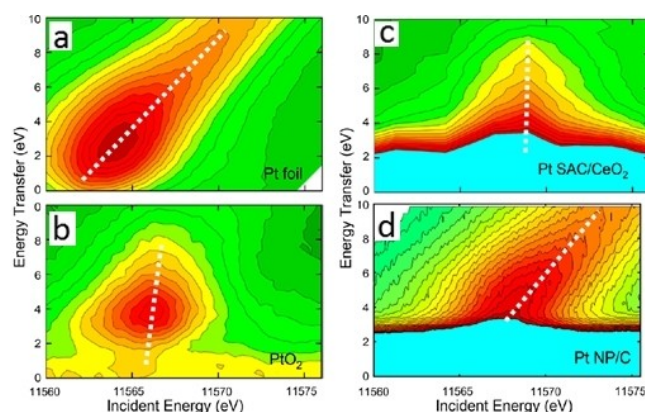


Figure 8. RIXS planes measured across Pt L₃ edge for (a) Pt foil and (b) PtO₂ standards, (c) Pt single atoms on CeO₂ and (d) Pt NPs on carbon from a previous work. Figure 8. (a–c), reproduced with permission from ref. [21]. Copyright 2019 American Chemical Society; Figure 8. (d), reproduced with permission from ref. [33a]. Copyright 2014 WILEY-VCH, Weinheim.

(dd) states. When the valence states of metals change with the external environment, the RIXS features will also change in accordance with the attributes of charge exchange involved. While RIXS measurements have been used to study nanosized catalysts,^[33] there are relatively few RIXS studies reported for single atom catalyst systems. The main challenge here arises due to the very low mass loading of the single metal atom sites being examined.

Recently, Kottwitz et al. studied the d state features of Pt single atoms supported on a nanoscale ceria material and the results showed the modified d states of Pt single atoms that arise due to the metal-support interaction.^[21] In a RIXS map (Figure 8), the horizontal axis is the incident energy, scanned across the Pt L₃ edge energy (11564 eV). The vertical axis is the energy transfer representing the energy difference between the incident and emitted photon energies. The d state features at zero-energy transfer can be used to determine the nature of the single atoms present. For a Pt foil reference, the elastic peak and the valence-band excitations merge together, as expected for a case where the Fermi level lies within a partially filled band. For PtO₂, a material with a bandgap in the range of 1.3–1.8 eV, a gap is seen between the elastic peak (zero energy transfer) and the lowest unoccupied 5d electronic states, one corresponding to a gap between the unoccupied 5d and occupied 5d states, with the Fermi level lying in the gap. The merging of the elastic peak and the valence-band excitations has been reported to occur in a simulated Pt₃₇ cluster, a simulated Pt₆ cluster, and a 2 wt.% Pt/Al₂O₃ sample with a particle size about 1 nm, affirming the metallic electronic structure of small Pt clusters in these cases.^[33a,b] However, for both the Pt single atom sample and nanoparticles samples (Figure 8), the d band features lower than the 2 eV in energy transfer could not be observed due to the strong background from the elastic peak.

The shape of the dd transition (the transition between occupied and unoccupied d states) features can provide an alternative means to evaluate information on the local bonding environment in this case. For both the Pt foil and Pt nanoparticle sample in Figure 8, the contribution of the d band tails along the diagonal of the RIXS plane, which corresponds to a scan of the incident energy at the fixed emission energy. Such emission energy is associated with the transition between the occupied Pt 5d to Pt 2p levels. For PtO₂ and Pt single atoms sample, similar features are not observed; instead, the contribution of d band tails along the vertical axis due to the Pt 5d-O 2p transitions that occur at higher energy transfer, suggesting the localized character of their Pt 5d states. The similarity between the RIXS behavior in PtO₂ and Pt SAC sample validates this hypothesis because in both samples Pt is bonded to the O atoms.

2.3. Local Coordination Environment

Numerous researchers have highlighted the role that the local coordination environment of SACs plays on their activity. Ren et al. developed a synthetic method to control the coordination

environment of Pt single atoms on a Fe₂O₃ support.^[17] In this method, they use ethanediamine to chelate Pt cations and then remove it by a rapid thermal treatment (RTT) in an inert atmosphere. By varying the RTT temperature from 500 °C to 600 °C while keeping the RTT time at 1 min, they obtained a series of Pt₁/Fe₂O₃-T samples (Figure 9(a)). As observed in EXAFS spectra (Figure 9(b)), with an increase of the RTT temperature, there is a decrease found in the amplitude of the Pt–O/N peak. More specifically, with the increase of the RTT temperature (500 °C, 525 °C, 550 °C, 575 °C, 600 °C), the coordination number of Pt–O decreases from 3.8, 3.1, 2.8, 2.0 to 1.8 (the error bar here was large, corresponding to about ±20%). Corresponding with these results, the white line intensities in the XANES spectra (Figure 9(c)) gradually decreased indicating a progressive reduction of the Pt single atoms. The average oxidation state of Pt single atoms in different Pt₁/Fe₂O₃-T catalysts were quantified basing on the XPS results (Figure 9(d)). For all the samples, Pt²⁺ and Pt⁰ coexist and the ratio of Pt²⁺ to Pt⁰ decreases with the increase of the RTT temperature. With the increase of the RTT temperature (500 °C, 525 °C, 550 °C, 575 °C, 600 °C), the average oxidation state of Pt decreases from 1.74, 1.25, 1.04, 0.64, to 0.51. By using the chemoselective reduction of 3-nitrostyrene as a probe reaction, the catalytic performance of Pt₁/Fe₂O₃-T samples were characterized and correlated with the Pt–O coordination number and the average oxidation state. As shown in Figure 9(e), as expected, there is linear relationship between the Pt–O coordination number and the average oxidation state: with the decrease of the Pt–O coordination number, the average oxidation state of Pt single atoms decreases. When correlating the structure properties with the catalytic activity (TOF), they also obtained an approximately linear relationship: the smaller coordination number of Pt–O, the lower oxidation state of Pt single atoms, the higher catalytic activity.

According to the DFT calculations (Figure 9(f)), on the two-coordinated Pt₁/Fe₂O₃-600 surface at 300 K, H₂ can dissociate spontaneously (the barrier of H₂ dissociation is 0). The barrier of H₂ dissociation on three-coordinated Pt₁/Fe₂O₃-550 is 0.25 eV, much lower than that on four-coordinated Pt₁/Fe₂O₃-500 (0.91 eV), indicating that the three-coordinated Pt₁/Fe₂O₃ catalyst is more active for H₂ activation than the four-coordinated Pt₁/Fe₂O₃-500. Under 300 K, the reaction energies for four-, three-, and two-coordinated Pt₁/Fe₂O₃ are –1.48, –1.71, and –1.87 eV, respectively. Hence, with the decrease in the Pt–O CN, it is much easier for Pt single atoms to activate H₂ molecules, making it several times more active in the hydrogenation reactions.

Ren et al.'s work shows that a strong correlation can exist between the coordination environment and the oxidation state of single atoms and that both of them can be used as descriptors for model catalytic reactions. On the other hand, the structural configuration itself could be the more essential feature related to activity.^[17] Zhao et al. performed a combined ab initio thermodynamics and DFT + *U* study to investigate the active site and reaction mechanism for the selective oxidation of methane to methanol on a ZrO₂-supported Rh single-atom catalyst. In agreement with Ren's work, the five-coordinated Rh

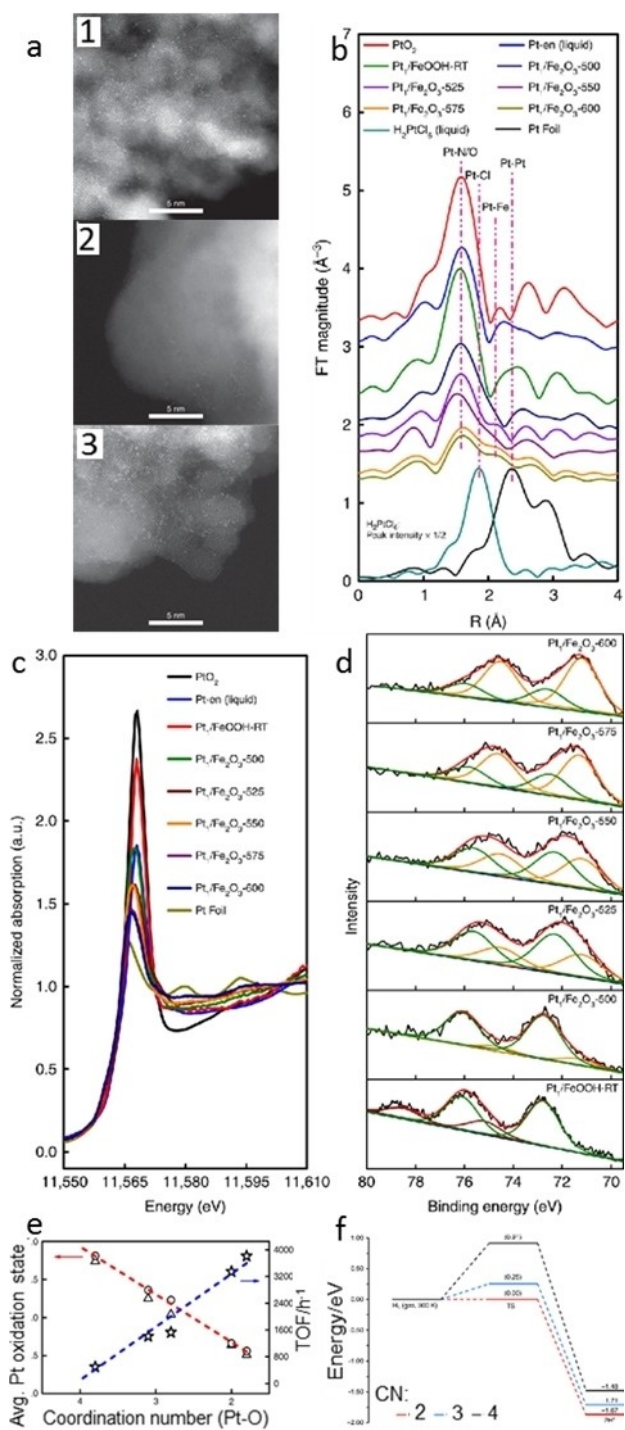


Figure 9. HAADF-STEM images of (a-1) Pt₁/Fe₂O₃-500 (a-2) Pt₁/Fe₂O₃-550 and (a-3) Pt₁/Fe₂O₃-600 catalysts. (b-d) The Pt L_{III}-edge XAS and Pt 4f XPS data of the Pt₁/Fe₂O₃-T catalysts. (b) The Fourier-transformed k^2 -weighted EXAFS spectra in R-space (without phase correction), (c) the normalized XANES spectra, (d) the Pt 4f XPS spectra. (e) The correlation between coordination structure and catalytic performance. The star, triangle, and circle represent TOF, average oxidation state of Pt determined from XPS and XANES, respectively. Linear correlations are obtained between the CN of Pt-O and the average oxidation state (red line), and between CN of Pt-O and the hydrogenation activity (blue line). (f) Energy profiles of H₂ dissociation on Pt₁/Fe₂O₃-T catalysts at 300 K. Four-coordinated Pt₁/Fe₂O₃-500 (black line), three-coordinated Pt₁/Fe₂O₃-550 (blue line), and two-coordinated Pt₁/Fe₂O₃-600 (red line) surfaces. Figure 9. (a-f), reproduced with permission from ref. [17]. Copyright 2019, The Author(s).

(+4.7) has higher oxidation state than the four-coordinated Rh single atoms (+3.6). The DFT results showed that the four-coordinated Rh can effectively stabilize the CH₃ species by suppressing its further dehydrogenation, whereas the five-coordinated Rh structure leads to an over-oxidation that prevents the formation of methanol. This is because the geometric configuration of CH₃ species at the four-coordinated Rh site hinders the interaction between H in the CH₃ moieties and neighboring O atom sites.^[34]

By controlling the local bonding of single Fe atoms, Pan et al. were able to improve the catalytic properties of so termed Fe-N_xC_y catalyst materials for benzene oxidation reactions (BOR), as illustrated in Figure 10.^[35] To prepare the Fe-N_xC_y catalysts with different Fe coordination environments, they applied a polymerization-regulated-pyrolysis (PRP) strategy: First, an iron-polyphthalocyanine (FePPC) conjugated polymer network was synthesized by a low-temperature solvent-free solid-phase method in muffle furnace; then the polymer network was subjected to pyrolysis at specifically regulated temperatures to afford the Fe-N_xC_y catalysts with different Fe-N coordination. At 500 °C, this procedure yields the benchmark Fe-N₄ SAs/N-C phase, at 600 °C, a Fe-N₃C₁ SAs/N-C variant, and at 700 °C, a carbide rich Fe-N₂C₂ SAs/N-C moiety (where N-C stands for the N-doped carbon matrix). To confirm the single-atom dispersion of the Fe and determine their electronic/atomic structures, STEM, XAS (at the C K edge, N K edge and Fe K/L edges), and XANES simulations were combined to characterize the as-prepared catalysts. The BOR performances of the as-prepared Fe-N_xC_y SAs/N-C catalysts were evaluated at 30 °C. The different Fe-N and Fe-C coordination environments lead to the different catalytic performances. The Fe-N₄ SAs/N-C catalyst exhibits the highest benzene conversion, phenol selectivity and stability, suggesting that the coordination environment play an important role in BOR. Theoretical calculations demonstrate the coordination pattern influences not only the structure and electronic features, but also the catalytic reaction pathway and the formation of key oxidative species. The increase of Fe-N coordination number facilitates

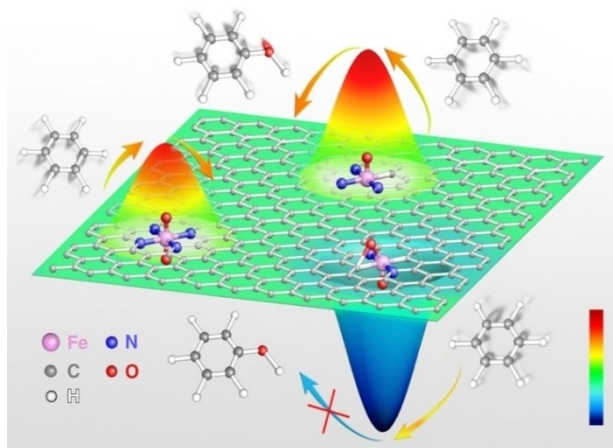


Figure 10. The schematic illustration to show the coordination effect of single-atom Fe-N_xC_y catalytic sites for benzene oxidation. Reproduced with permission from ref. [35]. Copyright 2019, The Author(s).

the generation and activation of the crucial intermediate $\text{O}=\text{Fe}=\text{O}$ species, thereby enhancing the BOR activity.

It is known that the strong cohesive energy and high surface free energy of single transition-metal atoms make them tend to sinter. This sintering can be mitigated by anchoring metals to the support via the metal-support interaction. The interaction between single atoms and the support depends on the physical properties of the specific metals and supports with attending features of bonding that determines their oxidation states, the charge distribution between them, the characteristics of metal d states, and the geometry of the metal bonding configurations on the support. All these features reflect how strong/weak the metal-support interaction is and could be correlated with catalytic reactivities. As demonstrated in selected examples, they are all connected.^[7,29] For theoretical works, any calculations on the electronic properties and catalytic mechanisms are based on a specific geometry, that is, with known information on the structure and geometry, information on the oxidation state, charge distribution, as well as the features of d-band density of states involved. The question that remains then is: How might it be possible to determine the geometry of the nearest environment of supported single atoms without a-priori assumptions of bonding configurations?

Experimentally, the combination of electron microscopy and X-ray absorption are generally used to determine the local atomic structure around single atoms. For carbon-based materials, the position of the single atom and its local bonding structure could be clearly seen from the TEM/STEM images. Figure 11(a–f) shows two ubiquitous configurations of a single Fe atom residing at an armchair graphene edge. In the first case (Figures 11(a–c)), an Fe atom is incorporated into a five-atom ring forming a pentagon. In the second case (Figure 11(d–f)), an Fe atom is incorporated into a five-atom ring forming a distorted hexagon (the Fe atom substitutes a carbon atom in the hexagonal lattice). The respective DFT-calculated structures are shown in Figure 11(c, f).^[36] For oxide-supported single atom catalysts, STEM images are usually used to demonstrate the atomic dispersion of single atoms. Depending on the type of metal in the support and in the single atom, more information may be obtained. For example, Figure 11(g) shows the aberration-corrected high-angle annular dark-field scanning TEM (AC-STEM) image of $\text{Mo}_1/\text{Fe}_2\text{O}_3$, which shows that the Mo ions are atomically dispersed on the $\alpha\text{-Fe}_2\text{O}_3(001)$ surface.^[37] As further analyzed by the selected-area intensity surface plot and the corresponding structural model, the Mo ions are precisely anchored on the threefold hollow sites (the yellow circles in Figure 11(h)). Hence, each isolated Mo ion and one adjacent outermost surface Fe ion (denoted as Fe_{surf} in Figure 11(h)) with a distance of $\sim 2.9 \text{ \AA}$ in between are assembled as one dinuclear site (the red ellipse in Figure 11(h)). However, for some systems that the metal of the support is close to or heavier than that of single atoms, and for this reason further analyses based on the STEM images remain very challenging.

As noted above, XAS is an extremely useful means for confirming the atomic dispersion of single atoms and providing quantitative structural information regarding their bonding. In

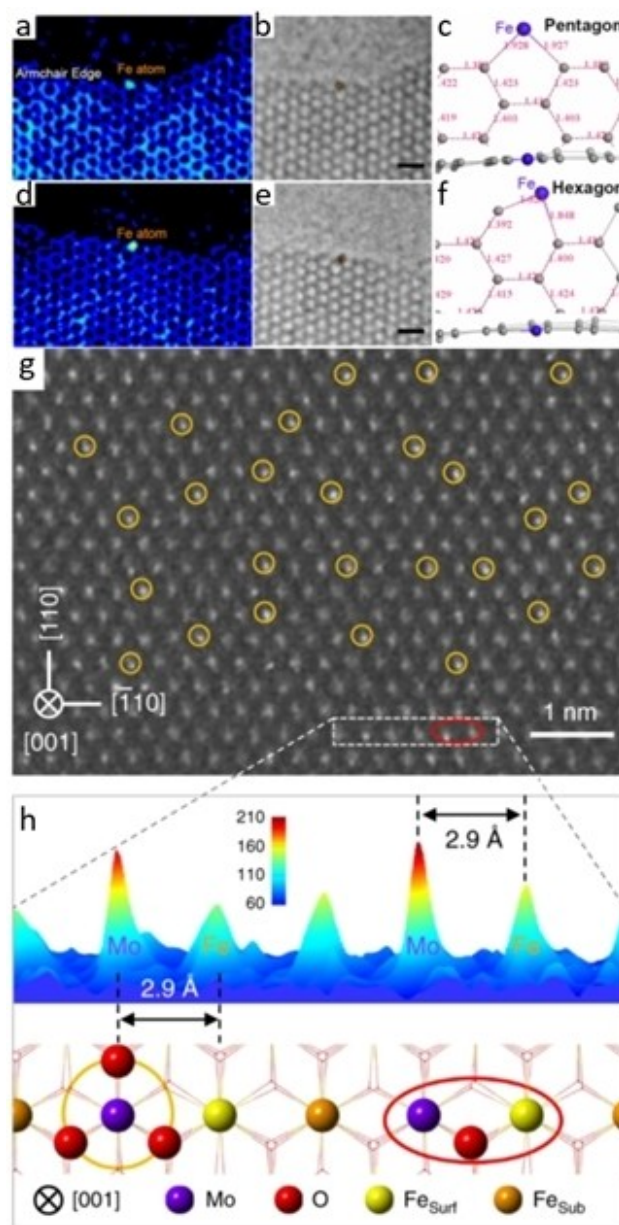


Figure 11. (a–c) High-resolution TEM (HRTEM) images (false color), magnified regions of HRTEM with overlaps of the DFT-calculated atomic structures, and DFT-derived structures (top and side views) of a pentagon including an Fe atom. Gray ball, carbon atom; orange ball, Fe atom. (d–f) HRTEM images (false color), magnified regions of HRTEM with overlaps of the DFT-calculated atomic structures, and DFT-derived structures (top and side views) of a distorted hexagon including an Fe atom. (Scale bars: b and e, 0.5 nm.) (g) AC-STEM image of $\text{Mo}_1/\text{Fe}_2\text{O}_3$. (h) Intensity surface plot and the corresponding structural model of the selected area (white dashed rectangle) in (g). Figure 11. (a–f), reproduced with permission from ref. [36]; Figure 11. (g, h), reproduced with permission from ref. [37]. Copyright 2020, The Author(s).

Ren's exemplary work discussed above, Pt–O coordination numbers were obtained from XAS analyses and in turn further correlated with the oxidation state of Pt and its catalytic activity.^[17] For systems with strong metal-support interactions, knowing only information about the nearest neighbor bonding interactions of the single atoms is not enough. O'Connor et al.^[31a] for example found that a $\text{Ir}/\text{CeO}_2(111)$ system charac-

terized by a strong metal-support interaction, there is significant charge transfer from the iridium adatom to neighboring oxygen and cerium atoms: two cerium atoms are reduced by the formation of an Ir^{2+} state. Whereas the adsorption of iridium onto CeO_2 involves the interaction between neighboring oxygen and cerium atoms, the metal-support interactions from the adsorption of iridium onto $\text{MgO}(100)$ are localized onto one surface oxygen atom.^[31a]

The information about the second nearest neighbors to the single atoms could also help determine/refine the three-dimensional geometry of single atoms on the support. As an example, Kottwitz et al. recently studied the electronic and atomic structures of Pt single atoms on the nano-sized ceria support.^[21] This work shows the importance of a full multimodal approach (including STEM, DRIFTS, XAS, RIXS, XPS and DFT) for addressing the questions: (1) *is it a single atom system?* (2) *what is the charge state of the isolated metal sites/ions?* (3) *what is the nature of the nearest environment, including the local perturbations of the support?* The combination of STEM, DRIFTS and XPS results suggests that Pt atoms in suitably prepared samples are singly dispersed, and the oxidation state of Pt single atoms is $2+$. The valence band XPS and RIXS measurements show the strong and unique interaction between the single Pt atom and the ceria support. To determine the local atomic structure, XAS measurement was performed. As shown in Figure 12(a), the white line of a single atom sample is similar to that of PtO_2 , though the XANES spectrum of the single atoms sample shows distinct features in the energy range of 11570 to 11630 eV. Important differences between the spectra of the SAC and PtO_2 samples are also observed in the EXAFS region, ones that include: (1) in k -space spectra, in addition to the lower oscillation amplitude, the spectrum of the single atoms sample shows different shapes in the range of 6 to 9 \AA^{-1} ; and (2) in R -space, though each of the spectra for PtO_2 and SAC samples have a pronounced peak at about 1.5 \AA which is assigned to the Pt–O contribution. The PtO_2 data contains two additional pronounced peaks in the range of 2.5 to 4.0 \AA (contributed by the second coordination shell (Pt–Pt) and Pt–O–Pt–O–Pt linear multiple scattering paths). The spectrum of Pt foil in comparison also shows two peaks but in the region of 2.0 to 3.5 \AA , ones due to the contribution of the first nearest Pt–Pt scattering path. For the SAC sample, the R -space EXAFS spectrum also shows two peaks in the region of 2.0 to 3.0 \AA but with unique features: the intensity of the shorter R -space distance peak being less than the one at larger R values. The uniqueness could also be observed by comparing wavelet transform (WT)-EXAFS (Figure 12(b)) of the as-prepared Pt single atoms/ceria with reduced Pt cluster/ceria, Pt foil, and PtO_2 . The raw data examinations then suggest that the peaks between 2.0 to 3.0 \AA are not due to Pt–Pt contribution but due to most likely Pt–Ce contribution. Further EXAFS data analysis confirms the hypothesis and provides quantitative local structure information. The agreement of the fitted and experimental spectra was shown in Figure 12(a). The model includes three paths: Pt–O, Pt–Ce, and Pt–O. In the best fitting results, for the first nearest Pt–O path, the coordination number is 4.2 ± 0.1 , the bond distance is $1.995 \pm 0.002 \text{ \AA}$. For the second nearest Pt–Ce path, the

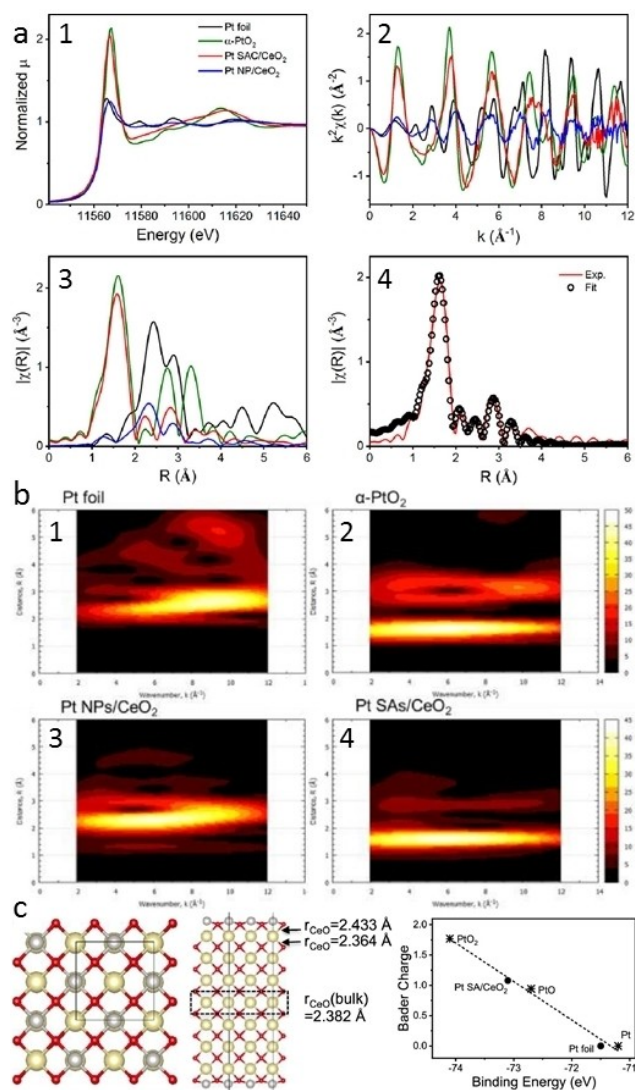


Figure 12. (a-1) Pt L_3 edge XAS spectra of Pt single atoms on ceria support. For comparison, the XAS spectra of standards (Pt foil and α - PtO_2) and ceria supported Pt nanoparticles (after reduction in H_2 of the PtO_x cluster on CeO_2 sample; reduction condition: 3.5% H_2 (balance He) at 423 K for 1 h; data were collected at room temperature after the treatment) are included. (a) XANES, (a-2) EXAFS spectra in k space, (a-3) EXAFS spectra in R space, and (a-4) comparison of experimental spectrum with the fit for the single atom sample. (b) Wavelet Transform (WT) – EXAFS of Pt foil, α - PtO_2 , Pt NPs/ CeO_2 , and Pt SAs/ CeO_2 data. (c-left) Top and side views of the Pt-passivated ceria (100) surface. The structure consists of Pt atoms occupying the hollow sites with 4 additional O atoms surrounding. Black lines indicate the unit cell. Pt: gray; Ce: light gold; O: red. The dashed box indicates the central O–Ce–O trilayer fixed at the bulk geometry. (c-right) Linear dependence of theoretical Bader charge on the Pt $4f_{7/2}$ core level binding energy for Pt, PtO , PtO_2 (asterisk markers), Pt single atoms on CeO_2 and Pt foil (dot markers). Dashed line is the linear fit. Figure 12. (a–c), reproduced with permission from ref. [21]. Copyright 2019 American Chemical Society.

coordination number is 4 ± 1 , and the bond distance is 3.34 ± 0.01 . These quantitative results, especially the Pt–Ce bond distance, aided DFT calculations for determining the three-dimensional geometry of Pt on ceria support.

Specifically for this complex case, we started from a previously reported structure, where a single Pt atom is placed on one of the (100) nanofaces of a cuboctahedral $\text{Ce}_{40}\text{O}_{80}$

nanoparticle (NP) in a truncated octahedral shape with O-terminated (111) and very small (100) nanofacets.^[38] In this PtCe₄₀O₈₀ NP model, the Pt atom is surrounded by four O atoms in a square shape with the Pt–O bond length of 2.05 Å, in reasonable agreement with the EXAFS results. There are four Ce atoms in the second shell; however, the Pt–Ce distance, however, turns out to be 3.05 Å basing on our calculations, a distance that is almost 9% shorter than the value of 3.34 Å value determined from the EXAFS data. Further investigations suggest that the underestimation of the Pt–Ce distance in tested models is attributed to the undercoordination of Ce atoms. Guided by this, the best structure model was obtained. As shown in Figure 12(c), in this model, Pt atoms fully passivate ceria (100) surface and occupy the hollow sites. The unit cell has stoichiometric CeO₂ plus 4 Pt atoms (two on each side) and 4 extra O atoms (Pt₄/O₄/CeO₂ (100)). Like the bulk, all the second shell Ce atoms in this model have a coordination number of 8. As a result, both the Pt–O bond length (1.987 Å) and Pt–Ce distance (3.32 Å) are in excellent agreement (within 0.5% relative error) with EXAFS measurements. Further analysis on the Bader charge suggests that in the best model, the Bader charge is 1.079, which is close to the value of 0.944 in PtO but far away from the value of 1.770 in PtO₂ (Figure 12(c)). Bader charge analysis indicates that the charge state of Pt in the ceria (100) model is close to +2, which agrees with the XPS finding.

2.4. Homogeneity versus Heterogeneity

It can be inferred from the discussions above that multiple single atom sites can coexist in a specific catalytic material system. The distinctions in this case reflect most centrally on attributes of metal-support bonding, valence states at sites associated with catalytic reaction mechanisms, rather than simply a dispersion of a specific metal at a single atom limit. Here for example, Thang et al. proposed that the potential candidates for a Rh SAC on ZrO₂ terrace sites are (RhO)_{ads} and (RhOH)_{ads} species.^[39] The presence of multiple speciations in heterogeneous samples complicates the interpretation of spectroscopic data that contain information about structural/compositional speciations that emerge as averages over the larger volume of the sample.

Our discussion regarding the experimental identification of heterogeneity in binding sites of single atoms in a sample begins with the techniques most commonly employed for single atom characterization: STEM, XPS, XAS and DRIFTS. The resolution of STEM instruments has been advanced to a level that now makes it possible to identify features of the speciations of an individual atom catalyst active site against the background of a support material. There are, however, several limitations in the ability of STEM imaging to provide quantitative structural information. The most important form of complexity arises in consequence of the STEM images being most commonly the result of a 2D projection of their actual 3D structure. Single atom materials also are often quite sensitive to radiation damage from the electron beam, causing atoms to migrate on surfaces or induce other structural changes. The

suitability of a sample for STEM imaging is influenced by the Z-contrast (or lack thereof) between the metal and support atoms. Care must also be taken in the identification of the surface facets on which the single atom(s) are located as the viewing axis is not necessarily indicative of the exposed surface facets.

XPS is another widely used characterization technique that probes the electronic structure of surface localized species. With regards to determining heterogeneity/homogeneity of single atom species, analysis of XPS data more readily allows for the confirmation of heterogeneity in surface speciation through the fitting of multiple peaks corresponding to the oxidation states of an element within the sample depth probed by the spectroscopy. While oxidation state homogeneity is perhaps the most desired correlate for the confirmation of speciation homogeneity, it does not in and of itself confirm a speciation as being homogeneous as multiple chemical structures may in fact be possible for SAC metal atoms that all the same bear the same oxidation state. For example, a PtO₂ nanoparticle will have a uniform Pt⁴⁺ oxidation state, but numerous different speciations such as edge sites, face/facet planes, and interior/bulk-like sites.

XAS is an element specific technique that probes the local coordination environment by observing the fluctuations in absorption arising from the multiple scattering paths of an ejected photoelectron. Fits made of the resultant spectra yield the average interatomic distances and coordination numbers of the local atomic structure for all species present within the sample. For a homogeneous speciation, it follows that the fitted parameters are representative of the probed environment of every SAC element. In contrast, the fitting of a heterogeneous sample yields a weighted average over all species of the X-ray absorbing atoms. Determination from XAS of whether a sample is heterogeneous or homogeneous requires knowledge of the expected/plausible/possible coordination environments and deconvolution of the experimental spectra to assign contributions to the multiple species present. This is often not possible.

To demonstrate that an ensemble-average XAS spectrum cannot be understood in terms of some representative, “effective” structure when the unique sites are inequivalent in terms of their local symmetry, we present the following example using theoretically generated XANES spectra. We considered three speciations of Co on CeO₂ as illustrated in Figure 13(a–c). Modeling of each species’ characteristic XANES spectra with FEFF (Figure 13d) demonstrates the unique spectroscopic features that arise from the particular electronic structure and local geometry of the SAC metal atoms. In the case of a homogeneous sample, identification of the speciation present becomes an exercise in matching the experimental spectra with that provided by modelling (or previously identified structures). For heterogeneous samples, the observed experimental spectra correspond to a weighted average of the spectra for each constituent speciation (examples of differently weighted “structure averaged” spectra are given in Figure 13 e). Solving an inverse problem of deconvolution average spectra is often very difficult if not impossible because it is generally ill-posed and not generally deterministic (no clear knowledge of unique species and their spectra may exist).

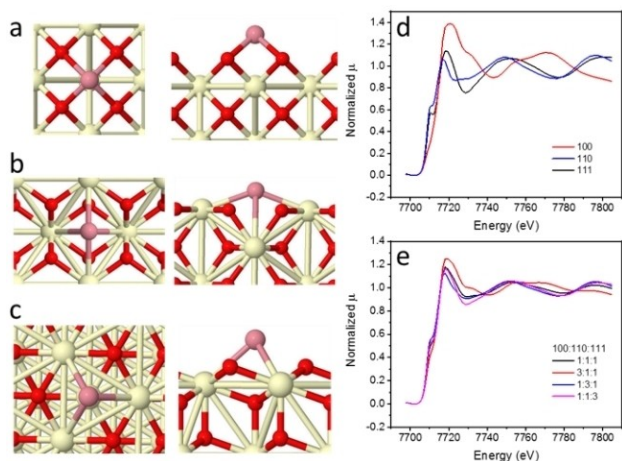


Figure 13. Schematics of an isolated Co atom on the (a) (100), (b) (110), and (c) (111) surface facets of CeO_2 . Simulation of their XANES spectra (d) demonstrates how the differences in local structure give rise to unique spectroscopic signatures. Weighted averages (the weighting fractions are given in the legend) of the modeled spectra (e) demonstrate how the presence of multiple speciations in a sample complicates their interpretation.

We illustrate approaches to consider such complexity via an example taken from our recent work, studies of a 0.1 wt.% Co/ CeO_2 SAC that was characterized by XAS. The raw data, collected at beamline 20ID of the Advanced Photon Source (APS), are shown in Figure 14. As shown in Figure 14a, for Co/ CeO_2 , the position of the rising edge is close to that of CoO. Except for that, the XANES spectrum of Co/ CeO_2 shows a unique set of distinguishing features. These include: a main peak at about 7723 eV; a shoulder at about 7727 eV and a low amplitude peak at about 7737 eV. Taken together, the data suggests that a local structure around the Co sites in Co/ CeO_2 that is different from that found in bulk Co, CoO, or Co_3O_4 . As shown in Figure 14b, the low R peaks for Co/ CeO_2 , ones due to Co–O contribution, are found between 1–2 Å. The Co–Co contribution at about 2 Å seen for a Co foil and at about 2.5 Å in CoO are not observed in the data for Co/ CeO_2 . The peak observed at about 3 Å is by inference one due to the Co–Ce contribution. To confirm the peak assignments and extract quantitative structural information, detailed EXAFS analyses were performed. These analyses were performed using Co–O and Co–Ce first and second nearest neighbors (other models,

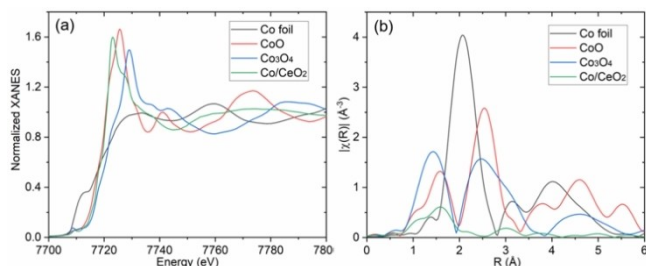


Figure 14. (a) The normalized XANES and (b) R space EXAFS spectra of 0.1 wt.% Co/ CeO_2 catalyst. The spectra of Co foil, CoO and Co_3O_4 are included for comparison.

such as Co–O and Co–Co, resulted in an inferior fit quality), consistent with Co being atomically dispersed on/in the ceria support. However, due to the high disorder of the Co–O bonds, the coordination number of Co–O obtained (3.8 ± 0.6) via the EXAFS fitting is underestimated by a significant amount. This suggests there could be multiple Co single sites present in the sample, each contributing to the averaged XAS signal.

It is possible in this case to take advantage of the unique spectroscopic features of the XANES data to deduce likely attributes of the structures that generate them. To do so for the Co/ CeO_2 SAC, XANES simulations were performed to determine the possible configurations of Co single atom sites. The simulations were made using FEFF9. The parameters were optimized by first simulating the spectrum of CoO and then applied in simulating the spectra of possible models of specific Co single sites, the structures for exemplary cases are shown in Figure 15. The models explore different exposed surface facets of CeO_2 , numbers of oxygen vacancies, and locations of Co. Candidates were first considered for their plausibility based upon the interatomic distances and coordination numbers found from the EXAFS fitting as shown in Figure 15. XANES simulations were then conducted for those candidates found to be in good agreement with the EXAFS fitting parameters. Two models, Co substituted for a Ce atom with a proximal O vacancy for the (111) surface facet and a bulk substitution of Co for Ce as shown in Figures 16a and b, were found to be in a very good

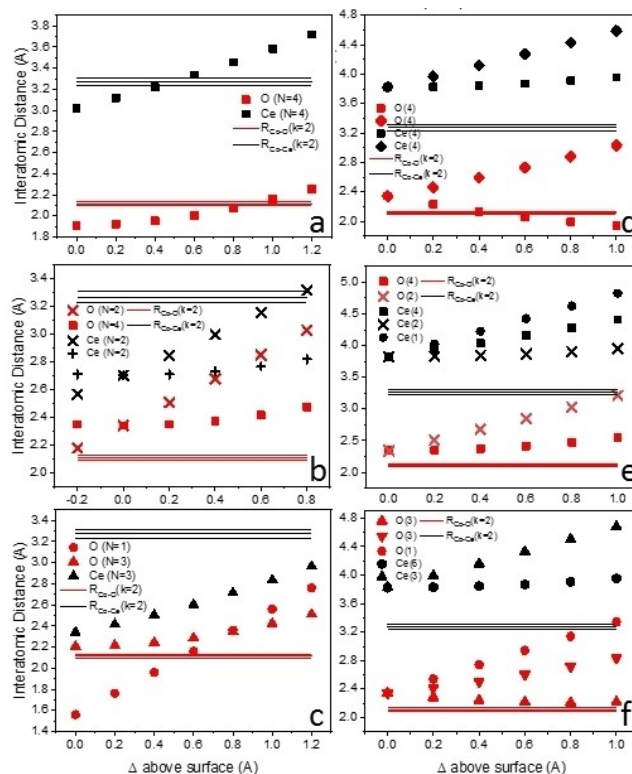


Figure 15. Comparison between experimental fitting results and modeled interatomic distances and coordination numbers for a selection of the considered speciations. (a–c) Co atoms on top of the (100), (110), and (111) surface facets, respectively. (d–f) Co atoms substituted for Ce atoms at the (100), (110), and (111) surfaces, respectively.

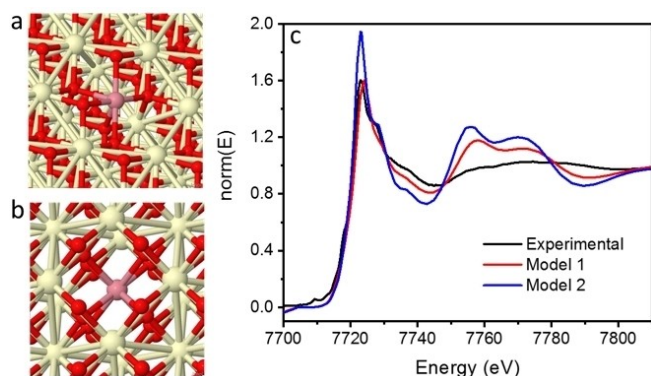


Figure 16. Models of (a) Co substituted for a Ce atom with proximal O vacancy for the (111) surface facet and (b) Co substituted for Ce in the bulk that were found to be in good agreement with the EXAFS fitting parameters. (c) Results of the XANES simulation for the two models considered and the experimental XANES spectra.

qualitative agreement with the experimental XANES spectra (Figure 16c). We point out also that a coexistence of several sites with different structural environments may result in a strongly asymmetric, or multimodal, pair distribution function $g(r)$, as was demonstrated in recent work by Gill et al.^[40] In this work, it was shown that Ni^{2+} was present in coexisting distorted tetrahedral and pentapyramidal environments, placements consistent with a strongly asymmetric $g(r)$ that resulted in the apparent EXAFS coordination numbers being significantly underestimated. We can in the present case, in analogy with the work by Gill et al.,^[40] propose a plausible interpretation of our hard to reconcile XANES and EXAFS data – that the data suggest the Co ions are heterogeneously distributed between Sites 1 and 2 in this supported SAC material.

A more local probe of SAC bonding characteristics that impact adsorbate interactions, one highly complementary to the insights from EXAFS, comes from DRIFTS, which provides chemical and structural information related to surface species, commonly through measurement of adsorbed probe (e.g., CO) molecules in studies of catalytic reaction mechanisms. The characteristic feature in the DRIFTS spectra of single atom catalysts using such a probe is a sharp/narrow peak that can be assigned to linearly adsorbed CO on an isolated metal atom site. Recent work has demonstrated that the full width at half-maximum (FWHM) of adsorbed CO stretching bands may serve as a tool to quantify the degree of uniformity present in the sample.^[41] This analysis assumes that, once the broadening due to finite lifetimes of the vibrationally excited probe molecule have been quantified, any additional broadening may be assigned to small shifts in vibrational frequency of the adsorbed species arising from variations as may be present in the adsorption sites or in consequence of neighboring species.

Sayler et al. were able to differentiate between the edge and interstitial sites for both Fe and Ni dopants in a [ZnAl]-layered double hydroxide, as illustrated in Figure 17a, using electron paramagnetic resonance (EPR) spectroscopy as part of a study modeling active sites for catalytic water oxidation.^[42] X-band continuous-wave EPR spectra were recorded at various

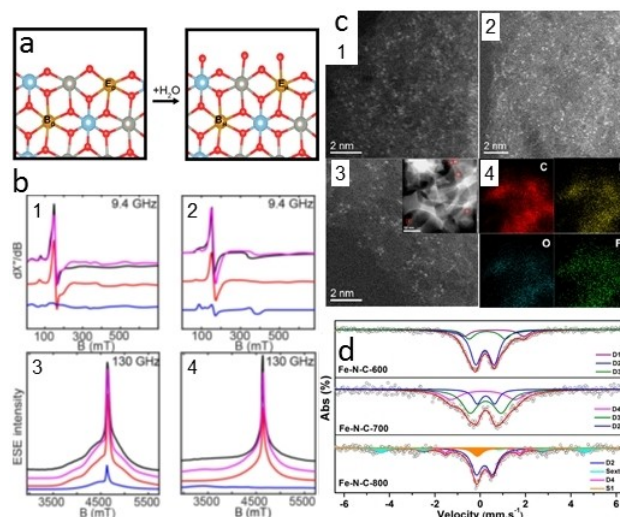


Figure 17. (a) Depiction of edge (E) and interstitial (B) sites of an NiFe layered double hydroxide under hydrated (H) and dehydrated (D) conditions (orange-iron/nickel, gray-zinc, light blue-aluminum, red-oxygen). (b) CW and pulsed spin echo spectra of hydrated [Fe:ZnAl]-LDH (left) and dehydrated [Fe:ZnAl]-LDH (right). Panels 1 and 2 at 9.4 GHz (30 K); panels 3 and 4 at 130 GHz (7 K). Simulation parameters: class B_H (red, panels 1 and 3) $S=5/2$, $g=2.003$, $D=0.20\text{ cm}^{-1}$, $E=0.044\text{ cm}^{-1}$; class B_D (red, panels 2 and 4) $S=5/2$, $g=2.003$, $D=0.19\text{ cm}^{-1}$, $E=0.050\text{ cm}^{-1}$; class E_H (blue, panels 1 and 3) $S=5/2$, $g=2.003$, $D=0.21\text{ cm}^{-1}$, $E=0.020\text{ cm}^{-1}$; class E_D (blue, panels 2 and 4) $S=5/2$, $g=2.003$, $D=-1.5\text{ cm}^{-1}$, $E=0.32\text{ cm}^{-1}$. The sum of the components is in magenta. (c) HAADF-STEM images of Fe-N-C-600 (1), Fe-N-C-700 (2), and Fe-N-C-800 (3) and elemental mapping of Fe-N-C-700 (4). The inset in part 3 shows the Fe-containing particles highlighted with red circles. (d) Mossbauer spectra of the Fe-N-C-600/700/800 samples. Figure 17. (a–b), reproduced with permission from ref. [42]. Copyright 2020, American Chemical Society; Figure 17. (c–d), reproduced with permission from ref. [43]. Copyright 2017, American Chemical Society.

temperatures under hydrated and dehydrated conditions as shown in Figure 17b. Parametrizing the spin Hamiltonian as a function of the electronic Zeeman energy, the zero-field splitting (ZFS) energy, axial contribution to the ZFS, and the rhombic contribution to the ZFS, allowed the authors to describe the coordination sphere of the metal centers by virtue of splitting only arising when ligands perturb the electronic structure of the metal center. At low concentrations (1–5%) the spectra demonstrated a sharp signal at 180 mT, a positive shoulder from 80 to 110 mT, and a negative feature at 80 mT. Simulation of the experimental spectra for the Fe sample was best modeled with two types of $S=5/2$ sites, that is, edge and interstitial sites. This approach of deconvoluting the experimental spectra into the contribution of each species mirrors our above discussion and provides an alternative method of demonstrating homogeneity/heterogeneity for applicable samples when other techniques are insufficient.

Liu et al.^[43] used Mossbauer spectroscopy to confirm the heterogeneity and identify the speciation of the Fe atoms present in a SAC sample as part of a study of nitrogen coordinated iron atoms on carbon support (Fe-N-C) for the selective oxidation of C–H bonds. These samples were prepared by pyrolyzing $\text{Fe}(1,10\text{-phenanthroline})_x$ supported on a nano-MgO template at temperatures ranging from 600 to 800 °C, followed by acid leaching to remove said template. Representa-

tive HAADF STEM images of the prepared samples are shown in Figure 17c. Assignment of the Mossbauer spectral features revealed a unique distribution of Fe speciations for each of the samples. As shown in Figure 17d, singlet and sextet components corresponding to γ -Fe and Fe_xC species, respectively, appeared only in the spectra of the sample pyrolyzed at 800 °C, indicating that the pyrolysis process produces atomically dispersed iron at 600 and 700 °C and nanoparticles of γ -Fe and Fe_xC at 800 °C. Comparison of the D4 doublet assigned to N-($\text{Fe}^{\text{III}}\text{N}_4$) species indicated that these unsaturated sites were present in greater abundance for the 700 °C sample in comparison to the 800 °C sample, while being absent for the 600 °C sample. Catalytic activity measurements combined with the area coverage determined by Mossbauer indicated that N-($\text{Fe}^{\text{III}}\text{N}_4$) is the most catalytically active species. For comparison, the N-($\text{Fe}^{\text{III}}\text{N}_4$)-N species (D3 doublet) was found to be 33 times less active due to the saturated and strong coordination of the central Fe atom with six neighboring N atoms. When taken together with the results from STEM, XPS and EXAFS measurements, the authors were able to identify the presence of heterogeneity in the samples, assign their speciation, and determine the most catalytically active species. This analysis again relies on the deconvolution of an observed spectra into contributions from individual components and provides an example of how one might determine the active species of a catalyst when said catalyst contains a heterogeneous speciation of the active element.

The exemplary cases presented above demonstrate two important considerations related to the study SAC materials. The first is the rather obvious one that SACs must present their active metal centers with the highest degree of dispersion that is possible for a heterogeneously supported transition metal catalyst – that each atom so supported is distinctly isolated from near neighbor interactions of a homometallic origin. The second consideration is one centered on the deeply challenging feature of how, and with what structural homogeneity, such metal centers are bonded in stable/active forms with a support phase and the consequences such features might have on catalytic properties. The latter frame a frontier challenge for research requiring multimodal means of characterization to address.

3. Summary and Outlook

The remarkable growth of interest in single atom catalysts in the last decade has been reflected in a rapidly growing number of reports in the literature on the synthesis of SAC systems, reactions in which they have demonstrated enhanced properties of activity/selectivity, along with methods for their characterization. This review has attempted to highlight the main challenges to understanding catalytic mechanisms of SACs as originate from the paucity of experimental methods that can provide quantitative insights into key physicochemical properties. These notably include: heterogeneity of binding sites of SACs on support; charge states; structural environments; and the associated tendencies towards changes in bonding/compo-

sition as might occur under reaction conditions. While we highlighted the strengths of various ex/in situ/operando techniques such as STEM, XPS, IR, and XAS for addressing these challenges, we also emphasized their limitations when used separately. We showed, using several examples from our own work and that of others, how specific combinations of techniques are required to provide reliable speciations of SACs, especially as they exist under reaction conditions. Even so, the extremely low metal loadings of SACs and the strong influence of the reactants and support continue to pose formidable challenges to X-ray methods that are predominantly model-dependent in their analytical ability to recognize various structural motifs. The advent of novel methods of XAS data analysis, such as those assisted by machine learning approaches,^[44] offer useful new capabilities in this regard. The materials diversity of SACs provides an excellent test of the validity of these and other approaches to monitor and decode *operando* structures in SACs.

Acknowledgements

Reaction tests and DRIFTS measurements at Brookhaven National Laboratory's Chemistry Division and XAFS data analysis were made possible due to the Program Development fund 21-017 to A.I.F. M.K. and R.G.N. acknowledge fellowship support from the Department of Chemistry at the University of Illinois. XAFS analysis work of A.I.F. was supported in part by the Catalysis Center for Energy Innovation, an Energy Frontier Research Center funded by the U.S. Department of Energy, Office of Science, Office of Basic Energy Sciences under Award No. DE-SC0001004. This research used resources of the Advanced Photon Source, a U.S. Department of Energy (DOE) Office of Science User Facility operated for the DOE Office of Science by Argonne National Laboratory under Contract No. DE-AC02-06CH11357.

Conflict of Interest

The authors declare no conflict of interest.

Keywords: catalysis · characterization · metal-support · single atom · structure-property

- [1] R. T. Hannagan, G. Giannakakis, M. Flytzani-Stephanopoulos, E. C. H. Sykes, *Chem. Rev.* **2020**, *120*, 12044–12088.
- [2] B. T. Qiao, A. Q. Wang, X. F. Yang, L. F. Allard, Z. Jiang, Y. T. Cui, J. Y. Liu, J. Li, T. Zhang, *Nat. Chem.* **2011**, *3*, 634–641.
- [3] a) S. Mitchell, E. Vorobyeva, J. Pérez-Ramírez, *Angew. Chem. Int. Ed.* **2018**, *57*, 15316–15329; *Angew. Chem.* **2018**, *130*, 15538–15552; b) C. Zhao, X. Dai, T. Yao, W. Chen, X. Wang, J. Wang, J. Yang, S. Wei, Y. Wu, Y. Li, *J. Am. Chem. Soc.* **2017**, *139*, 8078–8081; c) X. Li, W. Bi, L. Zhang, S. Tao, W. Chu, Q. Zhang, Y. Luo, C. Wu, Y. Xie, *Adv. Mater.* **2016**, *28*, 2427–2431.
- [4] Z. Zhang, Y. Zhu, H. Asakura, B. Zhang, J. Zhang, M. Zhou, Y. Han, T. Tanaka, A. Wang, T. Zhang, N. Yan, *Nat. Commun.* **2017**, *8*, 16100.
- [5] M. B. Boucher, B. Zugic, G. Cladaras, J. Kammert, M. D. Marcinkowski, T. J. Lawton, E. C. H. Sykes, M. Flytzani-Stephanopoulos, *Phys. Chem. Chem. Phys.* **2013**, *15*, 12187–12196.

- [6] J. Gao, H. b Yang, X. Huang, S.-F. Hung, W. Cai, C. Jia, S. Miao, H. M. Chen, X. Yang, Y. Huang, T. Zhang, B. Liu, *Chem* **2020**, *6*, 658–674.
- [7] X. Ye, H. Wang, Y. Lin, X. Liu, L. Cao, J. Gu, J. Lu, *Nano Res.* **2019**, *12*, 1401–1409.
- [8] S. Mitchell, J. Pérez-Ramírez, *Nat. Commun.* **2020**, *11*, 4302.
- [9] M. Li, H. Wang, W. Luo, P. C. Sherrell, J. Chen, J. Yang, *Adv. Mater.* **2020**, *32*, 2001848.
- [10] Q. Liu, Z. Zhang, *Catal. Sci. Technol.* **2019**, *9*, 4821–4834.
- [11] Y. Chen, Z. Huang, Z. Ma, J. Chen, X. Tang, *Catal. Sci. Technol.* **2017**, *7*, 4250–4258.
- [12] a) E. A. Derevyannikova, T. Y. Kardash, A. I. Stadnichenko, O. A. Stonkus, E. M. Slavinskaya, V. A. Svetlichnyi, A. I. Boronin, *J. Phys. Chem. C* **2019**, *123*, 1320–1334; b) J. Lee, Y. Ryou, X. Chan, T. J. Kim, D. H. Kim, *J. Phys. Chem. C* **2016**, *120*, 25870–25879; c) T. B. Li, F. Liu, Y. Tang, L. Li, S. Miao, Y. Su, J. Y. Zhang, J. H. Huang, H. Sun, M. Haruta, A. Q. Wang, B. T. Qiao, J. Li, T. Zhang, *Angew. Chem. Int. Ed.* **2018**, *57*, 7795–7799; *Angew. Chem.* **2018**, *130*, 7921–7925.
- [13] D. Kunwar, S. L. Zhou, A. DeLaRiva, E. J. Peterson, H. F. Xiong, X. I. Pereira-Hernandez, S. C. Purdy, R. ter Veen, H. H. Brongersma, J. T. Miller, H. Hashiguchi, L. Kovarik, S. Lin, H. Guo, Y. Wang, A. K. Datye, *ACS Catal.* **2019**, *9*, 3978–3990.
- [14] F. Dvorak, M. F. Camellone, A. Tovt, N. D. Tran, F. R. Negreiros, M. Vorokhta, T. Skala, I. Matolinova, J. Mysliveček, V. Matolin, S. Fabris, *Nat. Commun.* **2016**, *7*, 10801.
- [15] J. Y. Chen, Y. J. Wanyan, J. X. Zeng, H. H. Fang, Z. J. Li, Y. D. Dong, R. X. Qin, C. Z. Wu, D. Y. Liu, M. Z. Wang, Q. Kuang, Z. X. Xie, L. S. Zheng, *ACS Sustainable Chem. Eng.* **2018**, *6*, 14054–14062.
- [16] a) P. Chaudhuri, C. N. Verani, E. Bill, E. Bothe, T. Weyhermuller, K. Wieghardt, *J. Am. Chem. Soc.* **2001**, *123*, 2213–2223; b) N. Daelman, M. Capdevila-Cortada, N. Lopez, *Nat. Mater.* **2019**, *18*, 1215–1221.
- [17] Y. J. Ren, Y. Tang, L. L. Zhang, X. Y. Liu, L. Li, S. Miao, D. S. Su, A. Q. Wang, J. Li, T. Zhang, *Nat. Commun.* **2019**, *10*, 4500.
- [18] M. Moses-DeBusk, M. Yoon, L. F. Allard, D. R. Mullins, Z. L. Wu, X. F. Yang, G. Veith, G. M. Stocks, C. K. Narula, *J. Am. Chem. Soc.* **2013**, *135*, 12634–12645.
- [19] M. J. Hulse, B. Zhang, Z. R. Ma, H. Asakura, D. A. Do, W. Chen, T. Tanaka, P. Zhang, Z. L. Wu, N. Yan, *Nat. Commun.* **2019**, *10*, 1330.
- [20] a) K. Ding, A. Gulec, A. M. Johnson, N. M. Schweitzer, G. D. Stucky, L. D. Marks, P. C. Stair, *Science* **2015**, *350*, 189–192; b) F. Zaera, *Chem. Soc. Rev.* **2014**, *43*, 7624–7663.
- [21] M. Kottwitz, Y. Y. Li, R. M. S. Palomino, Z. Y. Liu, G. J. Wang, Q. Wu, J. H. Huang, J. Timoshenko, S. D. Senanayake, M. Balasubramanian, D. Y. Lu, R. G. Nuzzo, A. I. Frenkel, *ACS Catal.* **2019**, *9*, 8738–8748.
- [22] P. Bazin, O. Saur, J. C. Lavalley, M. Daturi, G. Blanchard, *Phys. Chem. Chem. Phys.* **2005**, *7*, 187–194.
- [23] J. Ke, W. Zhu, Y. Y. Jiang, R. Si, Y. J. Wang, S. C. Li, C. H. Jin, H. C. Liu, W. G. Song, C. H. Yan, Y. W. Zhang, *ACS Catal.* **2015**, *5*, 5164–5173.
- [24] Y. Sun, Y. Wang, J. S. Pan, L. L. Wang, C. Q. Sun, *J. Phys. Chem. C* **2009**, *113*, 14696–14701.
- [25] C. Lentz, S. P. Jand, J. Melke, C. Roth, P. Kaghazchi, *J. Mol. Catal. A* **2017**, *426*, 1–9.
- [26] E. Korin, N. Froumin, S. Cohen, *ACS Biomater. Sci. Eng.* **2017**, *3*, 882–889.
- [27] H. Thirumalai, J. R. Kitchin, *Top. Catal.* **2018**, *61*, 462–474.
- [28] B. Hammer, J. K. Nørskov, *Surf. Sci.* **1995**, *343*, 211–220.
- [29] J. Li, Q. Guan, H. Wu, W. Liu, Y. Lin, Z. Sun, X. Ye, X. Zheng, H. Pan, J. Zhu, S. Chen, W. Zhang, S. Wei, J. Lu, *J. Am. Chem. Soc.* **2019**, *141*, 14515–14519.
- [30] W. Chen, Y. Ma, F. Li, L. Pan, W. Gao, Q. Xiang, W. Shang, C. Song, P. Tao, H. Zhu, X. Pan, T. Deng, J. Wu, *Adv. Funct. Mater.* **2019**, *29*, 1904278.
- [31] a) N. J. O'Connor, A. S. M. Jonayat, M. J. Janik, T. P. Senftle, *Nat. Catal.* **2018**, *1*, 531–539; b) K. Tan, M. Dixit, J. Dean, G. Mpourmpakis, *Ind. Eng. Chem. Res.* **2019**, *58*, 20236–20246; c) S. K. Iyemperumal, T. D. Pham, J. Bauer, N. A. Deskins, *J. Phys. Chem. C* **2018**, *122*, 25274–25289.
- [32] L. J. P. Ament, M. van Veenendaal, T. P. Devereaux, J. P. Hill, J. van den Brink, *Rev. Mod. Phys.* **2011**, *83*, 705–767.
- [33] a) M. W. Small, J. J. Kas, K. O. Kvashnina, J. J. Rehr, R. G. Nuzzo, M. Tromp, A. I. Frenkel, *ChemPhysChem* **2014**, *15*, 1569–1572; b) P. Glatzel, J. Singh, K. O. Kvashnina, J. A. van Bokhoven, *J. Am. Chem. Soc.* **2010**, *132*, 2555–2557; c) J. A. v Bokhoven, C. Lamberti, in: *Nanotechnology in Catalysis* (Eds.: M. Van de Voorde, B. Sels), Wiley-VCH, Weinheim, **2017**, pp. 1029–1054.
- [34] Q. Zhao, B. Liu, Y. Xu, F. Jiang, X. Liu, *New J. Chem.* **2020**, *44*, 1632–1639.
- [35] Y. Pan, Y. Chen, K. Wu, Z. Chen, S. Liu, X. Cao, W.-C. Cheong, T. Meng, J. Luo, L. Zheng, C. Liu, D. Wang, Q. Peng, J. Li, C. Chen, *Nat. Commun.* **2019**, *10*, 4290.
- [36] J. Zhao, Q. Deng, S. M. Avdoshenko, L. Fu, J. Eckert, M. H. Rummeli, *Proc. Natl. Acad. Sci. USA* **2014**, *111*, 15641–15646.
- [37] W. Qu, X. Liu, J. Chen, Y. Dong, X. Tang, Y. Chen, *Nat. Commun.* **2020**, *11*, 1532.
- [38] A. Bruix, Y. Lykhach, I. Matolínová, A. Neitzel, T. Skála, N. Tsud, M. Vorokhta, V. Stetsovych, K. Ševčíková, J. Mysliveček, R. Fiala, M. Václavů, K. C. Prince, S. Bruyère, V. Potin, F. Illas, V. Matolín, J. Libuda, K. M. Neyman, *Angew. Chem. Int. Ed.* **2014**, *53*, 10525–10530; *Angew. Chem.* **2014**, *126*, 10693–10698.
- [39] H. V. Thang, G. Pacchioni, *ChemCatChem* **2020**, *12*, 2595–2604.
- [40] S. K. Gill, J. Huang, J. Matusz, R. Gakhar, S. Roy, F. Vila, M. Topsakal, W. C. Phillips, B. Layne, S. Mahurin, P. Halstenberg, S. Dai, J. F. Wishart, V. S. Bryantsev, A. I. Frenkel, *J. Phys. Chem. B* **2020**, *124*, 1253–1258.
- [41] a) J. Resasco, P. Christopher, *J. Phys. Chem. Lett.* **2020**, *11*, 10114–10123; b) A. S. Hoffman, C.-Y. Fang, B. C. Gates, *J. Phys. Chem. Lett.* **2016**, *7*, 3854–3860.
- [42] R. I. Saylor, B. M. Hunter, W. Fu, H. B. Gray, R. D. Britt, *J. Am. Chem. Soc.* **2020**, *142*, 1838–1845.
- [43] W. Liu, L. Zhang, X. Liu, X. Liu, X. Yang, S. Miao, W. Wang, A. Wang, T. Zhang, *J. Am. Chem. Soc.* **2017**, *139*, 10790–10798.
- [44] a) J. Timoshenko, A. I. Frenkel, *ACS Catal.* **2019**, *9*, 10192–10211; b) J. Timoshenko, D. Lu, Y. Lin, A. I. Frenkel, *J. Phys. Chem. Lett.* **2017**, *8*, 5091–5098; c) J. Timoshenko, S. Roese, H. Hövel, A. I. Frenkel, *Radiat. Phys. Chem.* **2020**, *175*, 108049; d) J. Timoshenko, C. J. Wrasman, M. Luneau, T. Shirman, M. Cargnello, S. R. Bare, J. Aizenberg, C. M. Friend, A. I. Frenkel, *Nano Lett.* **2019**, *19*, 520–529; e) J. Timoshenko, A. Anspoks, A. Cintins, A. Kuzmin, J. Purans, A. I. Frenkel, *Phys. Rev. Lett.* **2018**, *120*, 225502; f) J. Timoshenko, A. Halder, B. Yang, S. Seifert, M. J. Pellin, S. Vajda, A. I. Frenkel, *J. Phys. Chem. C* **2018**, *122*, 21686–21693; g) Y. Liu, N. Marcella, J. Timoshenko, A. Halder, B. Yang, L. Kolipaka, M. J. Pellin, S. Seifert, S. Vajda, P. Liu, A. I. Frenkel, *J. Chem. Phys.* **2019**, *151*, 164201; h) N. Marcella, Y. Liu, J. Timoshenko, E. Guan, M. Luneau, T. Shirman, A. M. Plonka, J. van der Hoeven, J. Aizenberg, C. Friend, A. I. Frenkel, *Phys. Chem. Chem. Phys.* **2020**, *22*, 18902–18910.

Manuscript received: March 2, 2021